

Contents lists available at ScienceDirect

International Journal of Plasticity

journal homepage: www.elsevier.com/locate/ijplas





Spatial and temporal evolution of localized deformation in NiTi tubes in a constant stress thermal cycle: Experiments and analysis

Solon Tsimpoukis, Stelios Kyriakides*, Chad M. Landis

Research Center for Mechanics of Solids, Structures & Materials, The University of Texas at Austin, Austin, TX 78712, United States

ARTICLE INFO

Keywords:
Shape memory alloys
Thermomechanical behavior
Isobaric cycle
Inhomogeneous deformation
Latent heat

ABSTRACT

A novel experimental setup is presented that allows for precise control of thermal and mechanical loads, and simultaneous monitoring of the temperature and the full-field deformation of small SMA structures that undergo phase transformations. The facility is used to conduct two experiments in which NiTi tubes are taken through a temperature cycle under constant load that leads to phase transformations in the form of helical localization bands that propagate along the specimen. The latent heat of transformation causes a complex interaction with the prescribed load and thermal environment. By changing the rate of the airflow through the environmental chamber it is revealed that the velocities of the transformation fronts depend on the rate at which heat is removed/added by the controlled environment. The experiments are simulated using a new fully coupled thermomechanical extension of the constitutive framework developed by this research group. Key features of the framework include the modeling of the reversible $A \rightleftharpoons M$ transformation through a single surface in the deviatoric stress-temperature space that obeys kinematic hardening; with the transformation strain and entropy as the internal variables governed by an associative flow rule; and the inhomogeneous deformation exhibited in tension being modeled as softening. The tube is analyzed in a finite element coupled static displacement transient temperature analysis, and taken through the cool/heat cycle of the experiment. The temperature-strain response is accurately reproduced with the two transformations initiating at essentially the same temperatures as in the experiment and propagating in similar localized banded manners at similar speeds. Reproduction of the complex behavior observed in the experiments requires the calibration of the constitutive model, its discretization, and the modeling of the structure and its boundary conditions to work together to near perfection. The simulation also demonstrated that the heat exchange between the structure and the environment, in the present analysis governed by only by convection, requires further enhancement.

1. Introduction

The unique properties of Shape Memory Alloys (SMAs) of *pseudoelasticity* and *shape memory effect* are derived from diffusionless solid-state transformations between two phases, *austenite* (A) and *martensite* (M). Since the transformations can be induced by either changes in temperature or stress, the material behavior is thermomechanically coupled (e.g., see reviews in Otsuka and Wayman, 1999; Lagoudas, 2008). The latent heat released/absorbed during transformation further adds to this coupling (e.g., Shaw and

E-mail address: skk@mail.utexas.edu (S. Kyriakides).

Corresponding author.

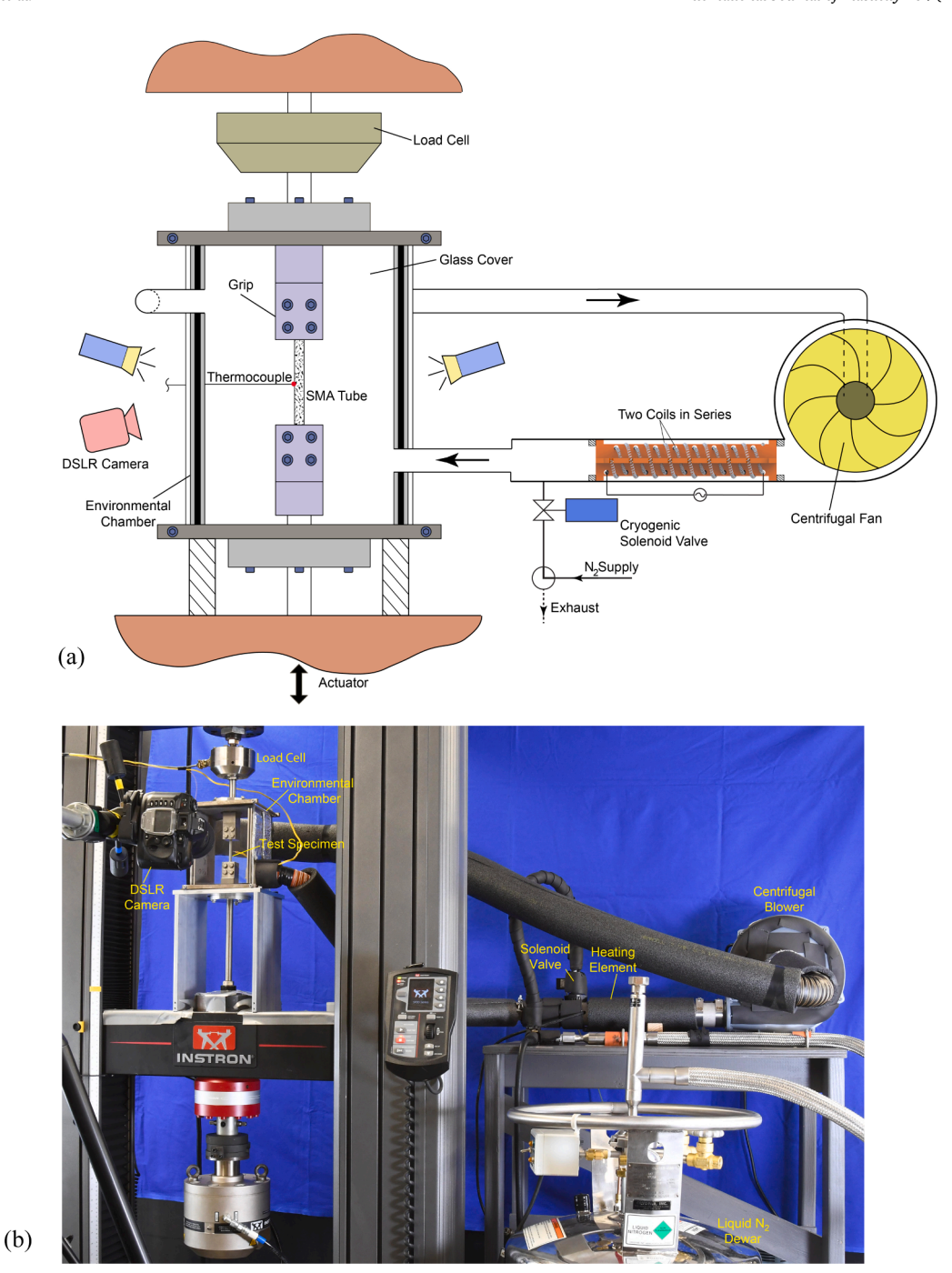


Fig. 1. The experimental setup developed for thermomechanical testing of materials and structures under controlled temperature and loading; used to conduct the isobaric experiments. (a) Schematic and (b) photograph, both with major components identified.

Kyriakides, 1997; Iadicola and Shaw, 2002, 2004; Favier et al., 2007; Pataky et al., 2015; Bechle and Kyriakides, 2016b; Li et al., 2021). Furthermore, the well-documented inhomogeneous deformation induced by the phase transformations (e.g., Shaw and Kyriakides, 1995, 1997; Iadicola and Shaw, 2002; Li and Sun, 2002; Daly et al., 2007; Mao et al., 2010; Bechle and Kyriakides, 2014; Reedlunn et al., 2014), the tension-compression asymmetry (e.g., Jacobus et al., 1996; Orgeas and Favier, 1998; Bechle and Kyriakides, 2014; Reedlunn et al., 2014; Jiang et al., 2016b), and in the case of sheet and tube stock material, anisotropy (e.g., Sun and Li, 2002; Bechle and Kyriakides, 2016a; Reedlunn et al., 2020), can challenge the design of SMA structures and devices. Constitutive models that address several of these complexities include: Boyd and Lagoudas, 1996; Lexellent et al., 2006; Levitas and Ozsloy, 2009a, b; Arghavani et al., 2010; Sedlack et al., 2012; Lagoudas et al., 2012; Jiang and Landis, 2016; Baxevanis et al., 2016; Li et al., 2021).

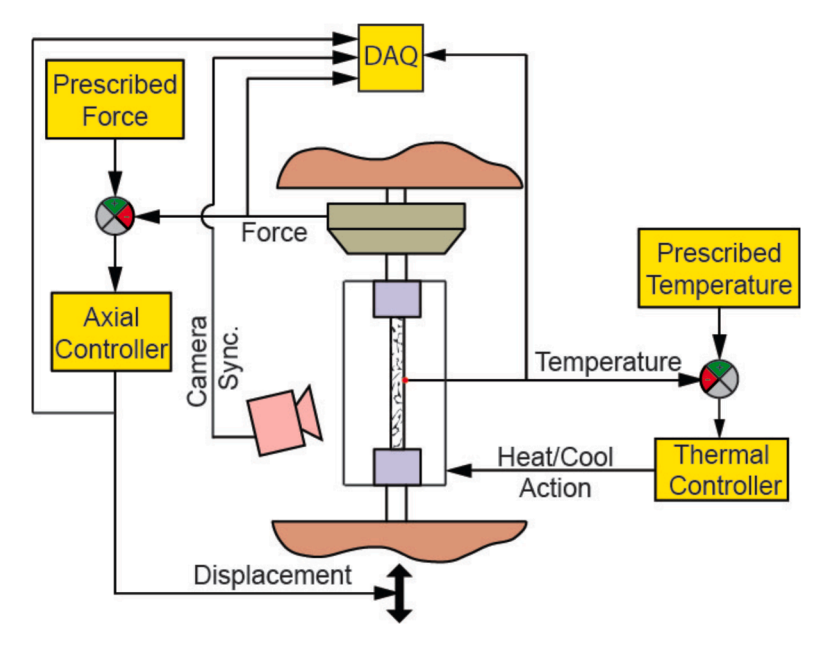


Fig. 2. Block diagram of data acquisition (DAQ) and feedback control systems for temperature and axial load.

In our past studies, concerned primarily with pseudoelastic behavior of NiTi, the thermomechanical coupling was alleviated by conducting both material and structural experiments under isothermal conditions (e.g., Shaw and Kyriakides, 1995; Bechle and Kyriakides, 2014, 2016a; Jiang et al., 2016a, 2017b). The isothermal pseudoelastic behavior of NiTi including the reversibility of transformation and the tension/compression asymmetry, was captured in a constitutive model in Jiang et al. (2016b) and Jiang and Landis (2016). Finite element analyses based on this constitutive model simulated successfully the response, localization, buckling and postbuckling behavior of tubular structures under tension, compression and bending (e.g., Jiang et al., 2016a, 2016b, 2017a, 2017b; Kazinakis et al., 2021, 2022).

More recently, our research extends this body of work to non-isothermal behavior of SMA structures. This paper introduces a custom testing facility suitable for thermomechanical experiments on SMA materials and simple structures under accurately controlled thermal and mechanical loadings at different rates. Here the facility is used to thermally cycle NiTi tubes under constant tensile stress. Such isobaric experiments have long been used to establish the transformation temperatures of materials at different stress levels (e.g., ASTM E3097-17, 2018). The precise control of both thermal and mechanical loads of the test facility, coupled with advanced diagnostics, enable a detailed monitoring of spatial and temporal evolution of localized deformations associated with the transformations.

The recent thermomechanical extension of the constitutive modeling framework developed by our research team presented in Alsawalhi and Landis (2022a), implemented as a material subroutine in a finite element analysis, is subsequently used to simulate two isobaric experiments. The performance of the analysis is evaluated by comparing the predictions to the experimental results and the comparison serves to inform both the experimental and modeling efforts about further developments.

2. Experimental set-up and procedure

2.1. Test facility for thermomechanical cycling

The test facility developed for controlled thermomechanical cycling of SMAs encompasses an insulated small-scale ($127 \times 127 \times 178 \text{ mm}-5 \times 5 \times 7$ in) environmental chamber that surrounds a test specimen mounted in an electromechanical testing machine as shown in Fig. 1. The specimen can be loaded under displacement, strain or load control. The specimen is speckled and its full-field deformation is monitored with digital image correlation (DIC). Its temperature field can be monitored with infrared radiometry by the insertion of infrared-transparent windows in the walls and by local thermocouples. Heating is provided by a stream of air heated by a 2 kW heating element with two concentric spirals of NiCr coils. Air is circulated by a variable speed centrifugal blower through an insulated closed loop as shown in Fig. 1. Cooling is accomplished by introducing N₂ vapor from a Dewar into the air stream controlled by a cryogenic solenoid valve. In the isobaric experiments presented here the temperature of the specimen is monitored by type K thermocouples in contact with the test specimen. A thermal cycle is tracked by a proportional integral derivative (PID) controller with the thermocouple temperature as feedback. The PID in turn actuates the heat/cool systems through a series of variable width pulses (PWM). This feedback loop is developed and operated in the LabView environment (see Fig. 2). The small size of the chamber and the relatively small thermal inertia of the overall system enable, for example, the accurate tracking of the prescribed 1.5 °C/min ramp throughout the -30 to 130 °C range of the facility.

Table 1Mean geometric dimensions and transformation temperatures of NiTi tubes used in the experiments.

D mm (in)	t mm (in)	$\frac{D}{t}$	A_s $^{ m o}{ m C}$	A_f $^{\circ}\mathrm{C}$	R _s °C	R_f $^{\circ}\mathrm{C}$	<i>M</i> _s °C
6.337 (0.2495)	0.269 (0.0106)	23.54	-9	11	8	-24	-65

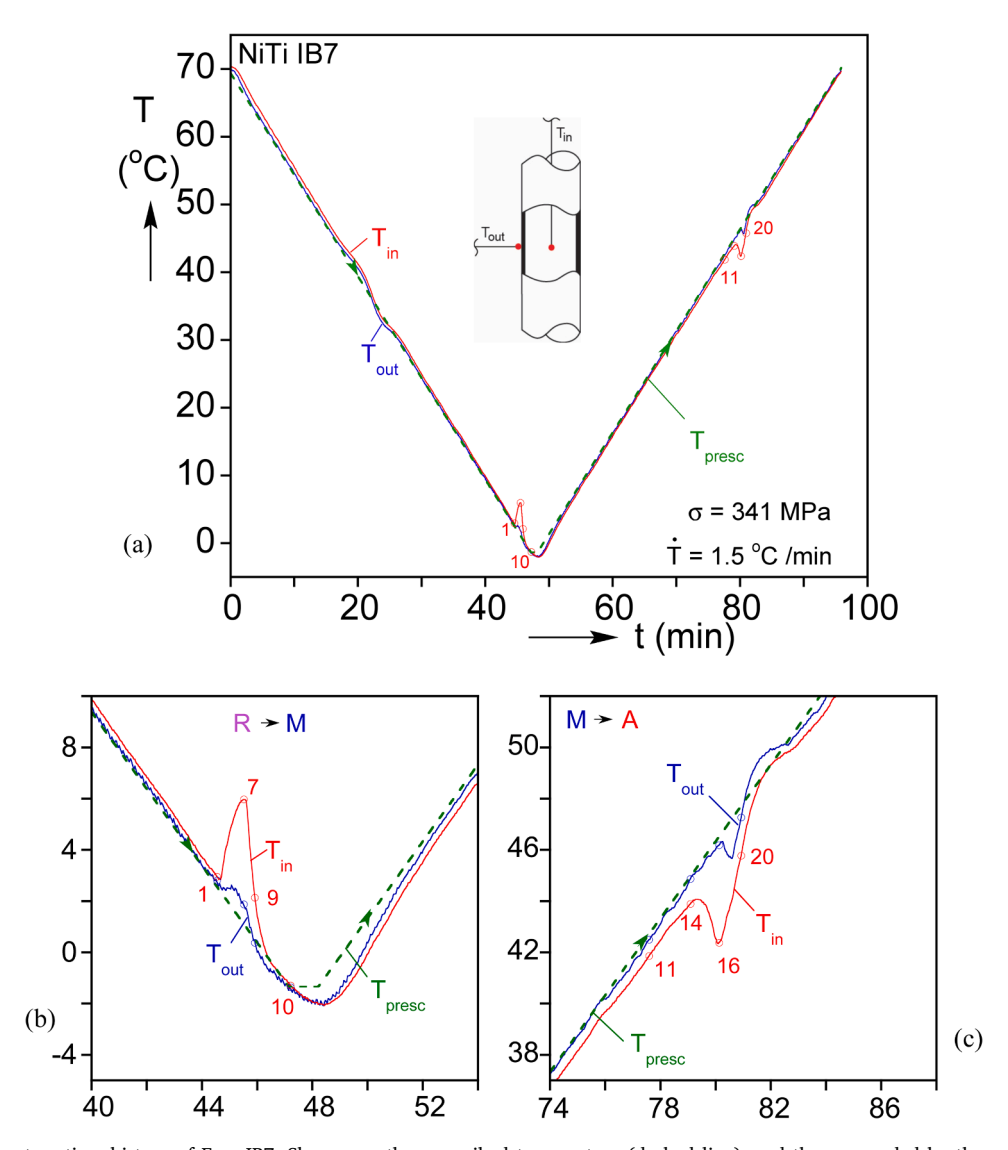


Fig. 3. Temperature-time history of Exp. IB7. Shown are the prescribed temperature (dashed line), and those recorded by the outer and inner thermocouple (solid lines). (a) Overall histories; (b) expanded histories during the R-M transformation; (c) expanded histories during the M-A transformation.

Data acquisition is performed via LabView through a sub-program that runs in conjunction with the thermal controller. Fig. 2 shows a block diagram of the overall data acquisition and control systems used in the isobaric experiments that follow. In these experiments the Instron 5982 testing machine is operated under load control using an external 22 kN (5 klb) load cell coupled to its load control loop. The stress stays at the prescribed level as the temperature goes through a cool-hold-heat cycle. The controller tracks the prescribed thermal path actuating the heat/cool systems as needed. The axial force, the frame displacement, and the thermocouple signals are continuously recorded at a rate of 5 Hz via LabView for later processing. Simultaneously, a 20 MP DSLR camera takes images of the deforming specimen at a prescribed rate with the images synchronized with the physical parameters monitored by DAQ.

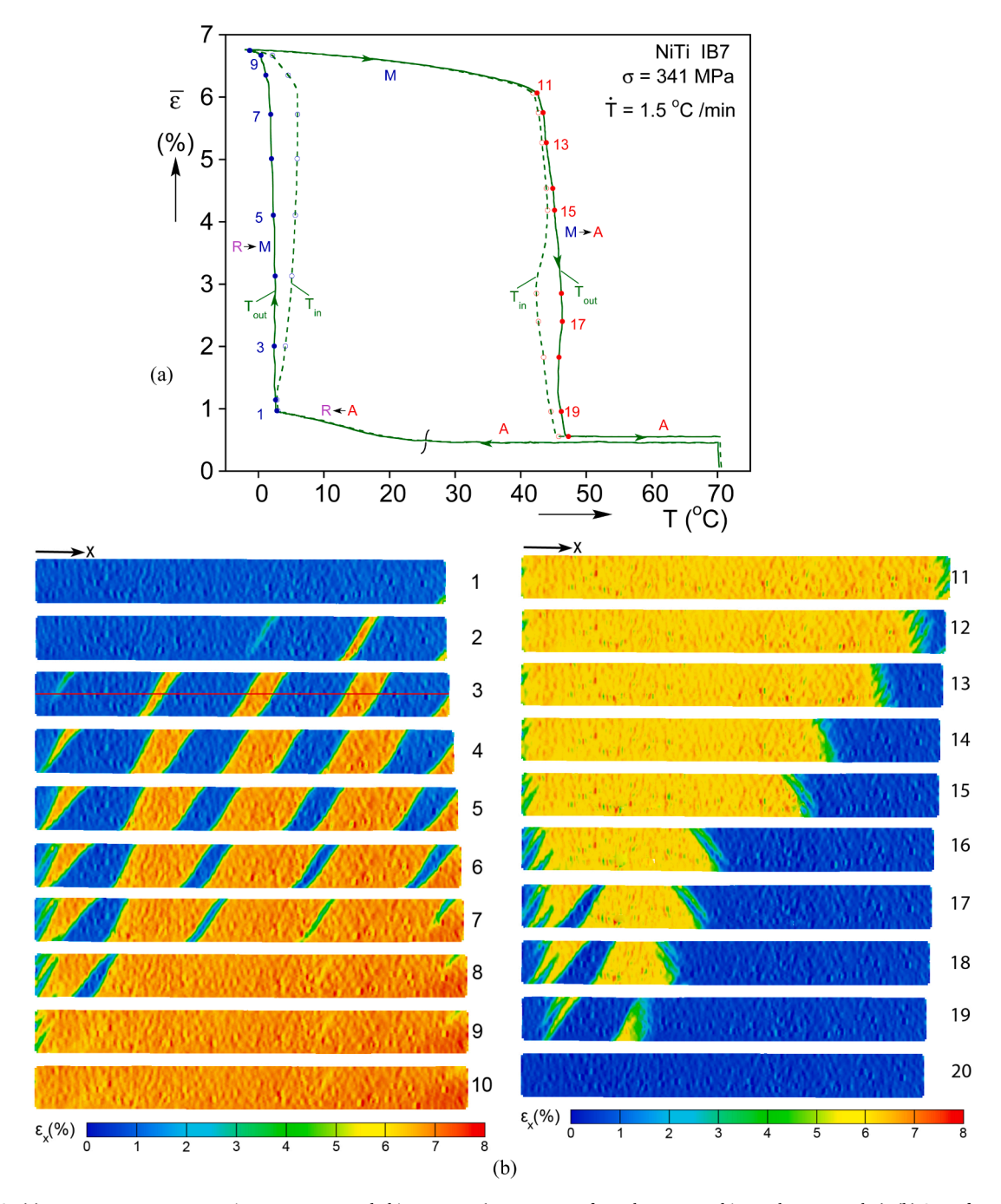
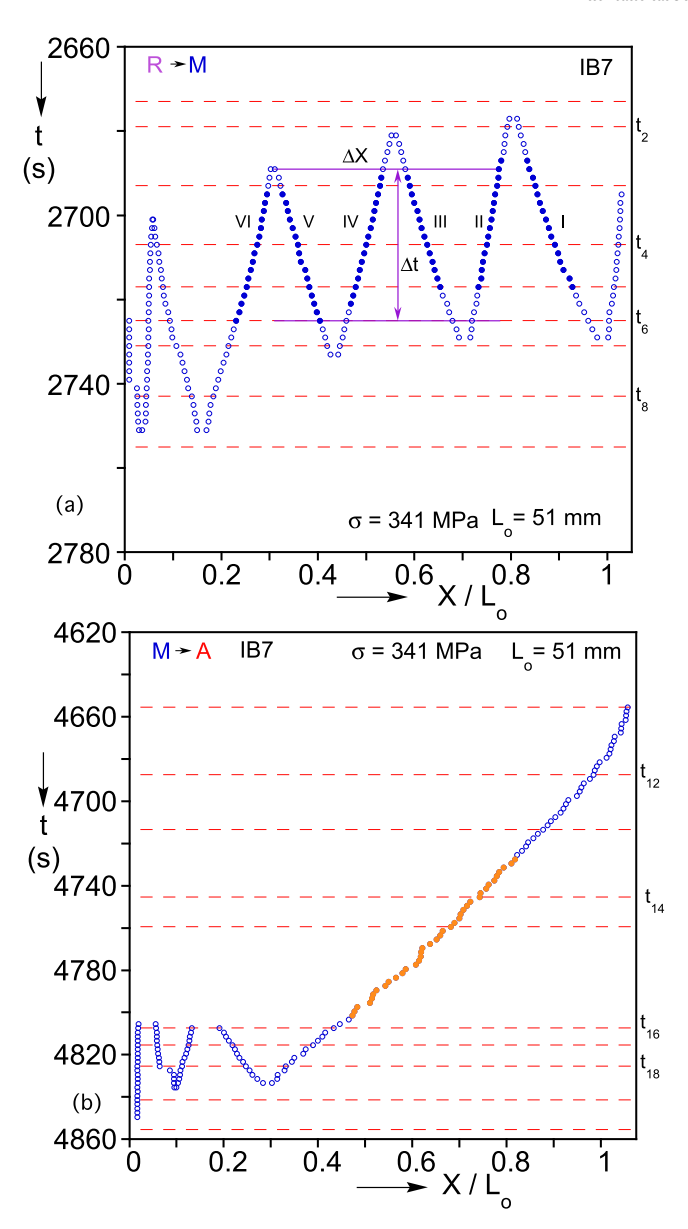


Fig. 4. (a) Temperature-average strain responses recorded in Exp. IB7 (temperatures from the outer and inner thermocouples). (b) Sets of specimen deformed configurations with axial strains superimposed corresponding to the R-M (left) and M-A (right) transformations.

2.1.1. Thermal cycling under constant stress – 341 MPa (Isobaric experiment, IB7)

The facility is now used to perform an *isobaric* experiment on a NiTi tube with the transformation temperatures listed in Table 1. Such tests are traditionally used to determine the transformation temperatures of materials at different stress levels (ASTM E3097-17, 2018). In the present experiments tubes with diameter 6.34 mm (0.25 in), diameter-to-thickness ratio of 23.54, and overall length of 127 mm (5.00 in) are taken through a cool/heat cycle under constant nominal stress of 341 MPa (49.45 ksi) (Table 1). The ends of the tubes are gripped using plate clamps with semi-circular notches leaving an exposed test section of 51 mm (2.0 in). Steel rods are inserted in the gripped ends to prevent crushing the tubes. The rods are hollow to allow the insertion of a thin thermocouple that monitors the inside temperature of the specimen (approximately at mid-span). A second thermocouple is in contact with the outer surface of the specimen at mid-span and is exposed to the flow stream (see Fig. 1a). The signal of this thermocouple is used as feedback



 $\textbf{Fig. 5.} \ \ \text{Deformed configuration positions} \ (X/L_o) \ \text{of transformation fronts vs. time} \ (t) \ \text{from Exp. IB7 for: (a) the R-M and (b) the M-A transformation.}$

to the thermal control loop (Fig. 2).

The prescribed ramp down-hold-ramp up temperature history for Exp. IB7 is plotted in Fig. 3a (dashed line). Included are the temperatures recorded by the feedback thermocouple (T_{out}) and by the one inside the tube (T_{in}). Overall, the two thermocouples track the prescribed temperature very accurately demonstrating the very good dynamic performance of the facility. A minor deviation from the prescribed temperature is observed during the ramp down between 40 °C and 30 °C when the system is transitioning from heating to cooling. The small transients that take place during the two-phase transformations are shown expanded in Fig. 3b and 3c and will be discussed below.

The two temperature records are plotted against the average axial strain $(T - \bar{\epsilon})$ in Fig. $4a - \bar{\epsilon}$ is the average strain over the field of view extracted from the DIC images. Two sets of deformed configurations of the test section with axial color strain contours superimposed are shown in Fig. 4b. They correspond to stations ①-⑩ and ⑪-⑳ marked with bullets on the response in Fig. 4a. Images ①-⑩ correspond to the R \rightarrow M and ⑪-㉑ to the M \rightarrow A transformation (henceforth A \equiv austenite M \equiv martensite, and R \equiv R-phase). The images demonstrate that both transformations lead to inhomogeneous deformation with the two phases co-existing. The deformation patterns are similar to those observed in isothermal displacement-controlled tension tests on tubes, (e.g., Fig. 2 Bechle and Kyriakides, 2014; Fig. 4, Bechle and Kyriakides, 2016a).

The temperature is first increased to 70 $^{\circ}$ C at a low stress (33 MPa). The stress is then set at 341 MPa and the temperature is ramped

Table 2 Velocities of fronts during the R \rightarrow M transformation in Exp. IB7 ($U_{flow} = 26 \text{ m/s}$).

	μm/s					
Front No.	I	II	III	IV	V	VI
\dot{X}	158.8	-81.18	139.4	-107.6	132.2	-107.6
$\frac{(\dot{X_i}-\dot{X_{i+1}})}{2},\;i=1,3,5$	120.0		123.5		119.9	
Average $-\dot{\bar{X}}$			1:	21.1		

down at a rate of 1.5 °C/min. The strain remains constant at about 0.47% down to about 30 °C – changes in length due to thermal contraction are small. A \rightarrow R transformation commences at about 25 °C leading to a gradual increase in strain reaching 0.96% at T=2.8 °C (station ①). The R-phase is a minor rhombohedral distortion of the cubic lattice of A. The distortion continues as the temperature decreases until the M-phase takes over at ① (e.g., Duerig and Bhattacharya, 2015). The resultant 0.5% deformation is homogeneous and so the latent heat released is effectively removed by the system, and no temperature disturbances are recorded.

a. $R \rightarrow M$ Transformation

M first nucleates in the specimen just before station ① as an angled finger of higher strain on the opposite side of the field of view. It emanates from the clamped end at the bottom (right in images) due to the inherent stress concentration – initiation site is just visible on the lower right corner of image ①. The nucleation causes the abrupt increase in the average strain observed in the $T - \bar{\epsilon}$ response. The finger initially propagates as a narrow sinistral helical band, which in image ② has propagated through half the length of the specimen – video IsobTemp_StrnExp.avi provides a more detailed exposé of the evolution of transformation in the specimen. The strain inside the band is about 6.5% while outside it remains at about 1%. The band makes an angle of about 59° to the axis of the tube (somewhat higher than the 55° predicted by Hill's (1952) analysis for uniaxial tension of thin walled tubes that exhibit Lüders-like localization, possibly due to anisotropy – see Bechle and Kyriakides, 2016a; Kazinakis et al., 2022). The band behind the propagating tip broadens as seen in images ③ and ④ when the tip reaches the left end and stops. Subsequent transformation is mainly by broadening of the helical band as observed in images ⑤ to ⑦ with $\bar{\epsilon}$ increasing from about 4% to about 5.7%. Band broadening is analogous to a two-front propagation, one toward the moving end (X = L) and a second toward the stationary end. The small island of mainly R on the left is transformed with a more compatible multi-pronged front seen in images ⑦ to ⑨ when transformation is essentially completed. Overall, the evolution of localized deformation is similar to that observed in displacement-controlled isothermal tensile tests on thin-walled NiTi tubes (Bechle and Kyriakides, 2016a).

The thermocouple inside the tube records a higher temperature than the outer one during phase transformation (Fig. 4a). The $R \rightarrow M$ transformation is exothermic and the released heat causes a small transient to the thermal response of the system that is shown expanded in Fig. 3b. In the case of the outer thermocouple, which is exposed to the airflow, the transient is quite small. Between stations ① and ⑦, T_{out} overshoots the prescribed linear trajectory by one degree. Subsequently, the temperature drops slightly below the prescribed value and returns to the prescribed trajectory by station ⑩. The thermocouple inside the tube is not in the flow stream and consequently reports a much larger temperature transient during the transformation. This difference between the two thermocouples is reflected in Fig. 4a.

The axial positions of the fronts observed in the 2-D DIC images at 2 s intervals are plotted in the X-t diagram in Fig. 5a (L_0 is the undeformed length of the test section; the axial position is measured at the mid-width of the specimen – see line drawn in image ③ in Fig. 4b). The zigzagging of the diagrams points out that for each section of the helical band one of its sides is propagating toward the moving end at X = L (forward, e.g., I, III, V), while its other toward the fixed end at X = 0 (backward, e.g., II, IV, VI). Appendix A outlines the kinematics of two fronts propagating toward each other (after Abeyaratne and Knowles, 2006). The velocities of the six fronts evaluated over the interval drawn with solid bullets are listed in Table 2, where the difference between the forward and backward velocities implied by Eqs. (A.2) is quite apparent. However, the average velocity of each pair of neighboring fronts is nearly the same. Interestingly, if the same calculations are performed in the undeformed configuration the average velocity is somewhat smaller as implied by Eq. (A.3) (difference \sim 7%).

We now select a central section of the domain of length ΔX , drawn with a solid line in Fig. 5a, and consider its elongation $\Delta \delta$ during the time period Δt identified in the figure. During this period the induced elongation is given by

$$\Delta \delta = n \dot{\bar{X}} \Delta \varepsilon' \Delta t,\tag{1}$$

where n=4 is the number of active fronts in this domain, \dot{X} is their average velocity from Table 2, $\Delta \varepsilon^t$ is the strain of the unstable part of the phase transformation, and $\Delta t=36$ s. The resultant $\Delta \delta=0.959$ mm. The elongation of this section during this time period was also evaluated directly from the full deformation field and found to be 0.928 mm, which confirms the fidelity of (1) (see also Shaw and Kyriakides, 1997, and references thereof).

It is important to point out that in a displacement controlled isothermal experiment the speed of the fronts is directly related to the prescribed δ . By contrast, in the present experiment run under constant stress and prescribed rate of change of temperature, the front speed is governed by the rate at which the latent heat released by the moving front is removed by the flow. This also enables the specimen temperature to better track the prescribed value. This somewhat complex thermomechanical interaction will be further

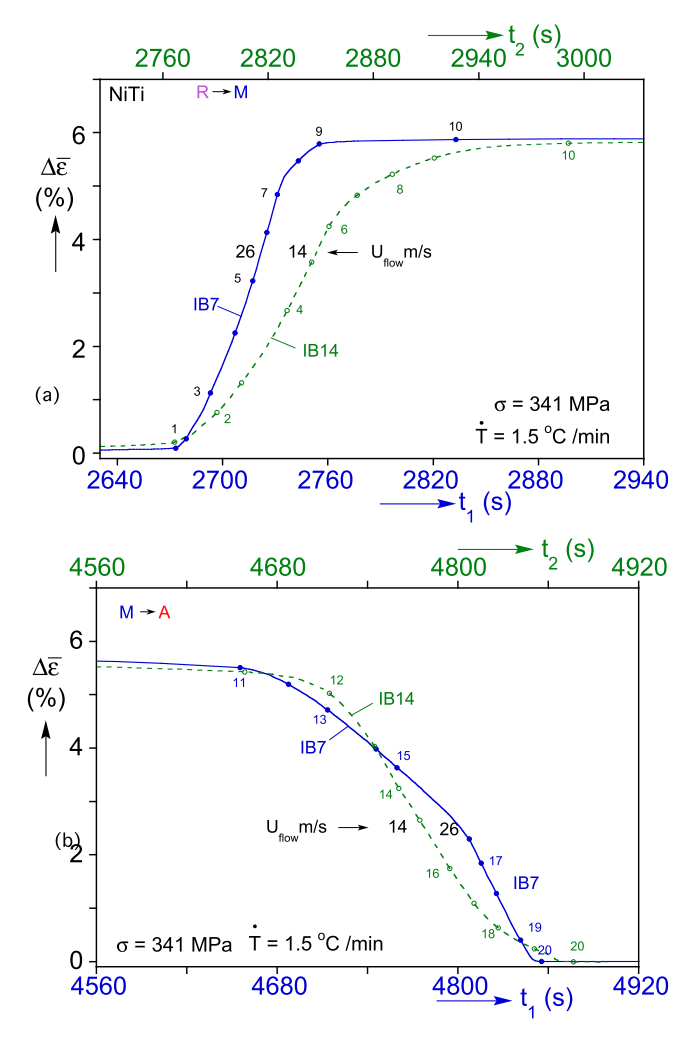


Fig. 6. Change of average strain vs. time during the transformations from Exp. IB7 for: (a) the R-M and (b) the M-A transformation.

scrutinized in light of the next experiment and numerical simulations that follow.

Fig. 6a shows the time history of the change in the <u>average</u> strain $\Delta \bar{\epsilon}$ in the test section during the 92 second duration of the transformation. Just prior to station ①, the testing machine accelerates resulting in a nearly constant strain rate between ② and ② that corresponds to the multi-front propagation observed in the FOV represented by front trajectories I to VI in Fig. 5a. With the appearance of the multi-pronged front on the left, the strain rate decreases and becomes zero after station ③. The cooling continues with $\Delta \bar{\epsilon}$ asymptotically reaching 5.8% and the overall strain $(\bar{\epsilon})$ 6.75% (Fig. 4a).

b. $M \rightarrow A$ Transformation

Following a brief hold, the temperature is ramped up as shown in Fig. 3a, and the resultant continuations of the two temperature-strain histories are included in Fig. 4a. The specimen deforms uniformly with the strain gradually decreasing to 6.15% at station \oplus . The decrease presumably is due to "uniformly" dispersed early transformation to A. In contrast to the sudden appearance of the single band of M at \oplus , localized transformation of A initiates rather gradually close to station \oplus with the nucleation of a multi-pronged front on the right end. It consists of sinistral prongs of about 0.5% strain (image \oplus). The evolution of the average axial position of the front is captured in the X-t diagram in Fig. 5b. The gradual acceleration of this front is reflected in its X-t trajectory between times t_{11} and t_{12} , and by the gradual decrease in $\Delta \bar{e}$ in Fig. 6b during the same time period. Around t_{13} the front starts to morph into an inclined one that is nearly fully formed by t_{15} . During the time period corresponding to the solid bullets in the X-t diagram in Fig. 5b, the band propagates at a nearly constant velocity of $-235 \,\mu\text{m/s}$, which is nearly double that of the fronts of the helical band discussed in Fig. 5a. However, during a period Δt of approximately 40 s, the front results in $\Delta \delta = 0.519 \,\text{mm}$ while the helical band in induces $\Delta \delta = 1.066 \,\text{mm}$ due to the multiplying effect of n = 4 in (1). Interestingly, between t_{16} and t_{19} when several transformation fronts are propagating, the rate of decrease in $\Delta \bar{e}$ increases significantly.

This transformation is endothermic so T_{out} and T_{in} record negative transients shown expanded in Fig. 3c. The single front

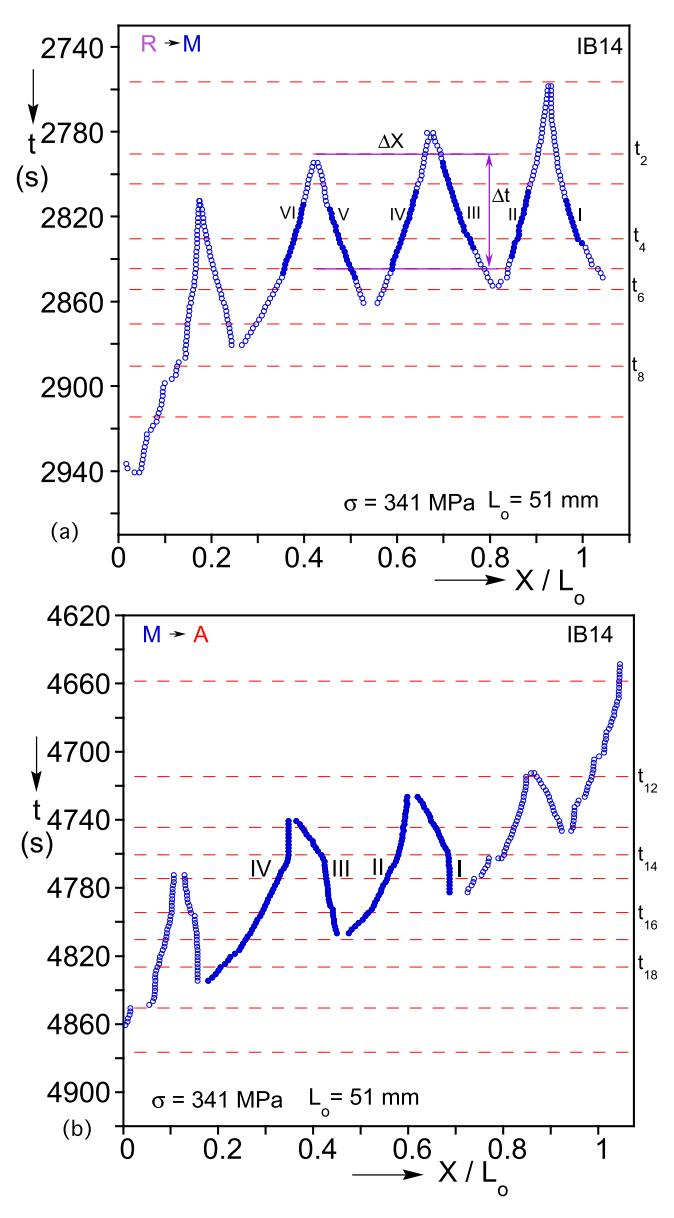


Fig. 7. Deformed configuration positions (X/L_0) of transformation fronts vs. time (t) from Exp. IB14 for: (a) the R-M and (b) the M-A transformation.

propagation implies that temperature drops are not registered in the neighborhood of the mid-span until after station 9 when the front is approaching. The maximum deviation from the prescribed value is once again small for T_{out} and about 3 °C for T_{in} . This difference is also reflected in the $T - \bar{\epsilon}$ responses in Fig. 4a. A new multi-prong front nucleates on the left end between stations 9 and 9. In image 9 a dextral helical band develops on the left, which propagates to the right while simultaneously broadening. The resultant increase in the number of moving fronts increases the rate of transformation of A and so $\Delta \bar{\epsilon}$ decreases at a faster rate in Fig. 6b. The helical band on the left meets the front propagating from the right just after image 9; the last island of M transforms causing the sharp corner in the response just prior to image 9 when the whole specimen is back to A. As the transformation moves away from the mid-span, the temperature at both thermocouples gradually returns to the prescribed value after station 9 (Fig. 3c).

In summary, M transforms to A primarily via a single front – initially multi-pronged and subsequently inclined – that propagates at nearly twice the speed at which the helical band fronts propagate during the $R \to M$ transformation. It induces a strain change of about 5.5%, and the event consumes 209 s (Fig. 5b), which is nearly twice the overall time of the $R \to M$ transformation. The main cause of this nearly doubling of the time of this event is the primarily single front propagation.

2.1.2. Isobaric experiment IB14

A second experiment was performed on the same tube in order to investigate the effect of the rate of heat transfer between the

Table 3 Velocities of fronts during the R \rightarrow M transformation in Exp. IB14 (U_{flow} =14 m/s).

	μm/s					
Front No.	I	II	III	IV	V	VI
\dot{X}	87.05	-60.58	83.35	-73.60	85.20	-68.60
$\frac{(\dot{X}_i - \dot{X}_{i+1})}{2} \ i = 1, 3, 5$	73.82		78.47		76.90	
Average			70	6.40		

specimen and the air stream on the results – IB14. To this end the velocity of the flow measured at the entrance to the chamber (see Fig. 1) was reduced from 26 m/s to 14 m/s while the axial stress was kept at 341 MPa and the rate of change of the prescribed temperature at 1.5 °C/min. The main results are broadly similar and are summarized in Appendix B. Fig. B1 plots the temperature-average strain response and corresponding deformed configurations, and Fig. B2 depicts the prescribed and the temperature histories of the two thermocouples. The $T - \bar{\epsilon}$ response follows closely the trajectory of IB7, with the temperatures at the onset and completion of transformations differing by 2–3°C. The overall thermal history (Fig. B2a) is the same, but some differences are observed in the temperature transients recorded during the transformations (Fig. B2b and B2c).

a. $R \rightarrow M$ Transformation

M nucleates at 1.0 °C in the form of a single helical band of high strain. The evolution of the band is broadly similar to that of IB7; however, its duration is now 236 s, which compares with 92 s for IB7. Fig. 7a plots the axial positions of the two sides of each band in the field of view at 2 s intervals in the form of a X-t diagram. The zigzag character of the plot is similar to that in Fig. 5a. The velocities calculated for each front are listed in Table 3. The trends are similar to those of IB7 in Table 2, however, the velocities are significantly lower, with the average velocity of 76.4 μ m/s being 37% lower. This slower evolution of the M-phase is also reflected in the $\Delta \bar{\epsilon} - t$ plot included in Fig. 6a where the average strain rate is seen to be significantly lower. It's worth pointing out that just after station \odot transformation switches to a single multi-pronged front, which slows down further the propagation of M, reduces the average strain rate, and adds to the overall time for its completion.

Evidently, the slower airflow is less efficient at removing the released latent heat. In order for the system to follow the prescribed stress and \dot{T} , the transformation speed slows down, causing a corresponding reduction in the rate of heat released, so that it matches the rate at which heat is removed by the slower airflow.

b. $M \rightarrow A$ Transformation

The M \rightarrow A transformation starts at 38 °C initially as a multi-pronged front at the right end, but by image @ reverts to a single helical band. This difference in the evolution of A from that of IB7 is reflected in the X-t of the front positions in Fig. 7b. The propagation of the helical band is somewhat "complex" with the velocities on the two sides alternating between slow and fast adding curvature to the trajectories. However, the average velocity of fronts I to IV is 73.2 μ m/s which is comparable to the 76.4 μ m/s value of the R \rightarrow M transformation. The overall time for this transformation is 225 s, which again compares well with the 236 s of the R \rightarrow M transformation. The $\Delta \bar{e} - t$ plot included in Fig. 6b exhibits a higher strain rate between stations @ and @, but a lower one at the beginning and completion of the transformation. Interestingly, the overall time of this event compares well with the 209 s duration of the corresponding transformation of IB7, which of course was through a single multi-pronged front. This near equivalence is once again caused by the slowing down effect on the transformation due to the decreased effectiveness of the heat transfer of the slower airflow.

The results of the two experiments demonstrate the following regarding the localized evolution of transformation:

- (i) In the present experiments heat transfer is governed by the flow of air through the environmental chamber. The velocity of propagation of transformation fronts decreases or increases so as to match the rate at which heat is removed by the slower/faster airflow.
- (ii) In the case of thin-walled tubes, single helical transformation fronts propagate at much slower speeds than single multi-pronged fronts.

3. Analysis

3.1. Constitutive model

The constitutive model adopted is based on the recent thermomechanical extension of Alsawalhi and Landis (2022a) (hitherto A&L2022a) of the framework first presented in Jiang et al. (2016b) and Jiang and Landis (2016). A key feature of the model is that the reversible $A \rightleftarrows M$ transformation is modeled through a single surface in the deviatoric stress-temperature $(s_{ij} - \theta)$ space that obeys kinematic hardening (in keeping with the notation of A&L2022a, here temperature is represented by θ). The transformation strain ε^t_{ij} and entropy S^t are assigned as the internal variables and their evolution is governed by an associative flow rule. The Helmholtz free energy is assumed to take the form:

$$\Psi = \frac{1}{2} c_{ijkl} \left(\varepsilon_{ij} - \varepsilon_{ij}^t \right) \left(\varepsilon_{kl} - \varepsilon_{kl}^t \right) - \beta_{ij} \left(\varepsilon_{ij} - \varepsilon_{ij}^t \right) (\theta - \theta_1)$$

$$+ C \left(\theta - \theta_1 - \theta \ln \frac{\theta}{\theta_1} \right) - \theta S^t + \Psi^t \left(\varepsilon_{ij}^t, S^t \right)$$
(2)

where c_{ijkl} are the elastic moduli, $\beta_{ij} = c_{ijkl}\alpha_{kl}$ are the thermal expansion moduli, C is the heat capacity per unit volume, ($C/\rho =$ specific heat, $\rho =$ mass density), θ_1 is a reference temperature, and Ψ^t is the hardening potential.

Application of the second law of thermodynamics (Gibbs, 1878; see also Valanis, 1970) to the problem can be expressed as:

$$\dot{\Psi} \le \sigma_{ij} \dot{\varepsilon}_{ij} - S \dot{\theta} - \frac{1}{\rho} q_i \theta_{,i},\tag{3}$$

where q_i is the heat flux and θ_{ij} is the temperature gradient. The stress σ_{ij} and entropy S derived from (2) are:

$$\sigma_{ij} = \frac{\partial \Psi}{\partial \varepsilon_{ij}} = c_{ijkl} \left(\varepsilon_{kl} - \varepsilon'_{kl} \right) - \beta_{ij} (\theta - \theta_1) \tag{4a}$$

and

$$S = -\frac{\partial \Psi}{\partial \theta} = \beta_{ij} \left(\varepsilon_{ij} - \varepsilon_{ij}^t \right) + C ln \left(\frac{\theta}{\theta_1} \right) + S^t$$
 (4b)

Inequality (3) then becomes

$$\left(\sigma_{ij} - \sigma_{ij}^{\mathsf{B}}\right) \dot{\varepsilon}_{ij}' + \left(\theta - \theta^{\mathsf{B}}\right) \dot{S}' - \frac{1}{a} q_i \theta_{,i} \ge 0,\tag{5}$$

where σ_{ij}^B and θ^B are the back stress and back temperature of the yield surface defined in the deviatoric stress-temperature space as given below:

$$\Phi = \frac{3}{2} \frac{\left(s_{ij} - s_{ij}^B\right) \left(s_{ij} - s_{ij}^B\right)}{\sigma_a^2} + \frac{\left(\theta - \theta^B\right) \left(\theta - \theta^B\right)}{\theta_a^2} - 1, \quad s_{ij} = \sigma_{ij} - \sigma_{kk} \delta_{ij} / 3,$$

$$(6)$$

where s_{ii}^B and θ^B are

$$s_{ij}^{B} = \frac{\partial \Psi^{i}}{\partial \varepsilon_{ii}^{I}} \text{ and } \theta^{B} = \frac{\partial \Psi^{i}}{\partial S^{i}}.$$
 (7)

The evolution of the internal variables is governed by the following flow rule

$$\dot{\varepsilon}'_{ij} = \lambda \frac{\partial \Phi}{\partial \widehat{S}_{ii}} \text{ and } \dot{S}' = \lambda \frac{\partial \Phi}{\partial \widehat{\Theta}}, \tag{8}$$

where $\hat{s}_{ij} = s_{ij} - s_{ii}^B$ and $\hat{\theta} = \theta - \theta^B$.

The heat flux follows Fourier's heat conduction law

$$q_i = -k\theta_{ij},\tag{9}$$

where k is the thermal conductivity.

The first law of thermodynamics (Alsawalhi and Landis, 2022b) can be written as:

$$\dot{U} = \dot{\Psi} + \dot{\theta}S + \theta \dot{S} = \sigma_{ii}\dot{\varepsilon}_{ii} - q_{i,i} + r, \tag{10a}$$

where \dot{U} is the internal energy density rate and r the rate of heat generated per unit volume – r = 0 in the present application. Introducing Ψ from (2), the first law becomes:

$$C\dot{\theta} = k\theta_{,ii} - \theta\beta_{ij} \left(\dot{\varepsilon}_{ij} - \dot{\varepsilon}'_{ij} \right) - \theta \dot{S}' + 2\lambda. \tag{10b}$$

Here $-\theta \dot{S}^{t}$ represents the latent heat of transformation and 2λ is the heat generation due to the hysteresis. After a complete $A \rightleftharpoons M$ transformation cycle the net contribution of the first term is zero while that of the second term is positive.

The transformation potential is chosen as (A&L2022a):

$$\Psi^{t} = \frac{H(\vec{\epsilon}^{t}/\varepsilon_{o})^{2}}{2\left(1 - \frac{\vec{\epsilon}^{t}}{\varepsilon_{o}} - \frac{S^{t}}{S_{o}}\right)^{n}} + \frac{H_{1}}{\left(1 - \frac{S^{t}}{S_{o}}\right)^{u}\left(\frac{S^{t}}{S_{o}}\right)^{v}} + \theta^{*}S^{t} + \frac{H_{2}}{2}\left[\left(1 - \frac{S^{t}}{S_{o}}\right)^{2} + \left(\frac{S^{t}}{S_{o}}\right)^{2}\right],\tag{11}$$

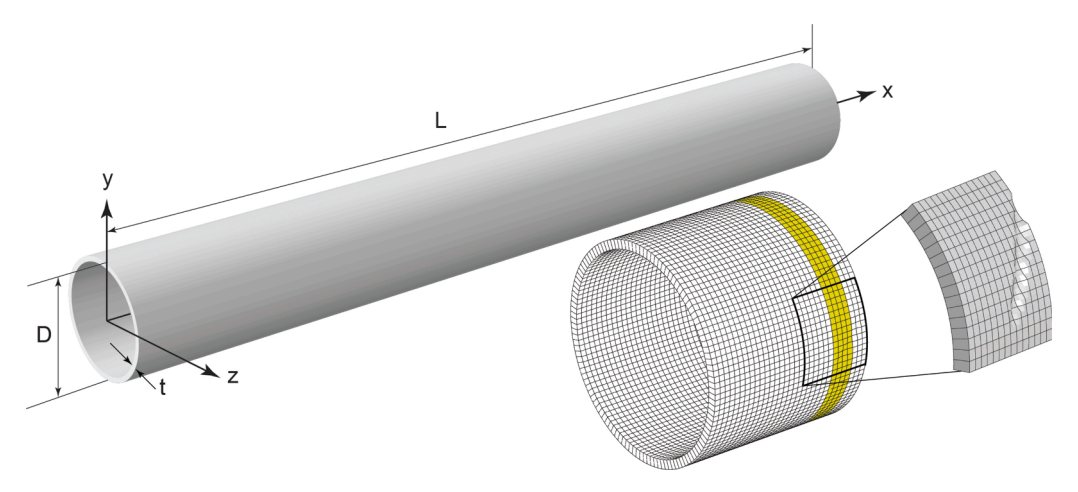


Fig. 8. Finite element model geometry and mesh. Shown expanded is the small thickness depression used to initiate the localized deformation induced by the transformation.

where
$$\bar{\varepsilon}^t = (2\varepsilon_{ii}^t \varepsilon_{ii}^t/3)^{1/2}$$
.

The model is calibrated to a set of isothermal pseudoelastic tensile responses and to the thermoelastic properties of the material as outlined in Appendix C. The model is discretized using the backward Euler method (Alsawalhi, 2022) and is implemented as a material subroutine in ABAQUS.

3.2. Finite element model

The two isobaric experiments on NiTi tubes are simulated numerically using a finite element model developed in ABAQUS. A tube of length L, diameter D, and wall thickness t, is meshed using second-order solid elements, C3D20RT with reduced integration. The dimensions of the model tube of $\{L,D,t\}=\{50.8,6.34,0.268\}$ mm are chosen to match those of the tube used in the experiment (see Fig. 8). A fine mesh is used with 120 elements around the circumference, 306 along the length and one through the thickness. As in our previous models of problems that develop localization patterns such as the ones observed in the experiments, the mesh density is chosen for good reproduction of the finer features of the anticipated localization patterns, while ensuring reasonable execution time. The localization is captured by the introduction of softening over the extents of the transformation (Appendix C). For this reason the sensitivity of the solution to the mesh was examined. As reported in our previous studies, the mesh does not influence the overall structural response or the patterns significantly (e.g., Jiang et al., 2017a, 2017b; Hallai and Kyriakides, 2011; Kazinakis et al., 2022). Its main effect is limited to controlling the width of the transition zone between high and low deformation regimes. Alternative schemes for handling unstable material behavior by the introduction of higher order strain gradients to the formulation have, for example, been reported in Rezaee-Hajidehi et al. (2020), Li et al. (2021), and Frost et al. (2021). Such approaches require calibration of the introduced length scale, and tend to increase the computational cost.

The "clamped" boundary conditions at the two ends of the tube are idealized as radially constrained by fixing the outer nodes of the edge elements. The axial displacement is restrained at x = 0 while the axial force is prescribed x = L, and kept constant throughout the simulation at the value that corresponds to the 341 MPa stress level of the experiment.

As in all our previous simulations of inelastic localization-type instabilities, a small thickness depression is introduced at x = L to help initiate the localization. The thickness imperfection, shown in the expanded end of the model in Fig. 8, is inclined by approximately 55° to the axis of the tube, has a semi-elliptical cross section, a width of t, depth of 0.1t, and extends approximately 4t from the end of the model. Because the actual boundary conditions in the experiment were more complicated than assumed here, it was found useful to apply in addition a pressure, P (10 MPa), to the outer surfaces close to the two ends over a ring 2.5t wide shown highlighted in the expanded image of the end at x = L in Fig. 8.

The outer surface of the model is assigned convection boundary conditions with the heat flux

$$q = h(T - T_{\infty}),\tag{12}$$

where h is the *convection coefficient* and T_{∞} the "sink" temperature prescribed to this surface (SFILM in ABAQUS – hereafter θ is replaced with T for consistency with the experimental results). T_{∞} is assigned the same cool-heat cycle used in the experiment at the rate of $\dot{T}_{\infty} = 1.5$ K/min. The inner surface of the model is insulated (q = 0).

The coupled thermomechanical structural problem is treated as static in terms of the displacement field and transient in terms of the temperature field. The partial differential equations that govern the two fields are the force balance and the energy balance (10b) represented respectively by

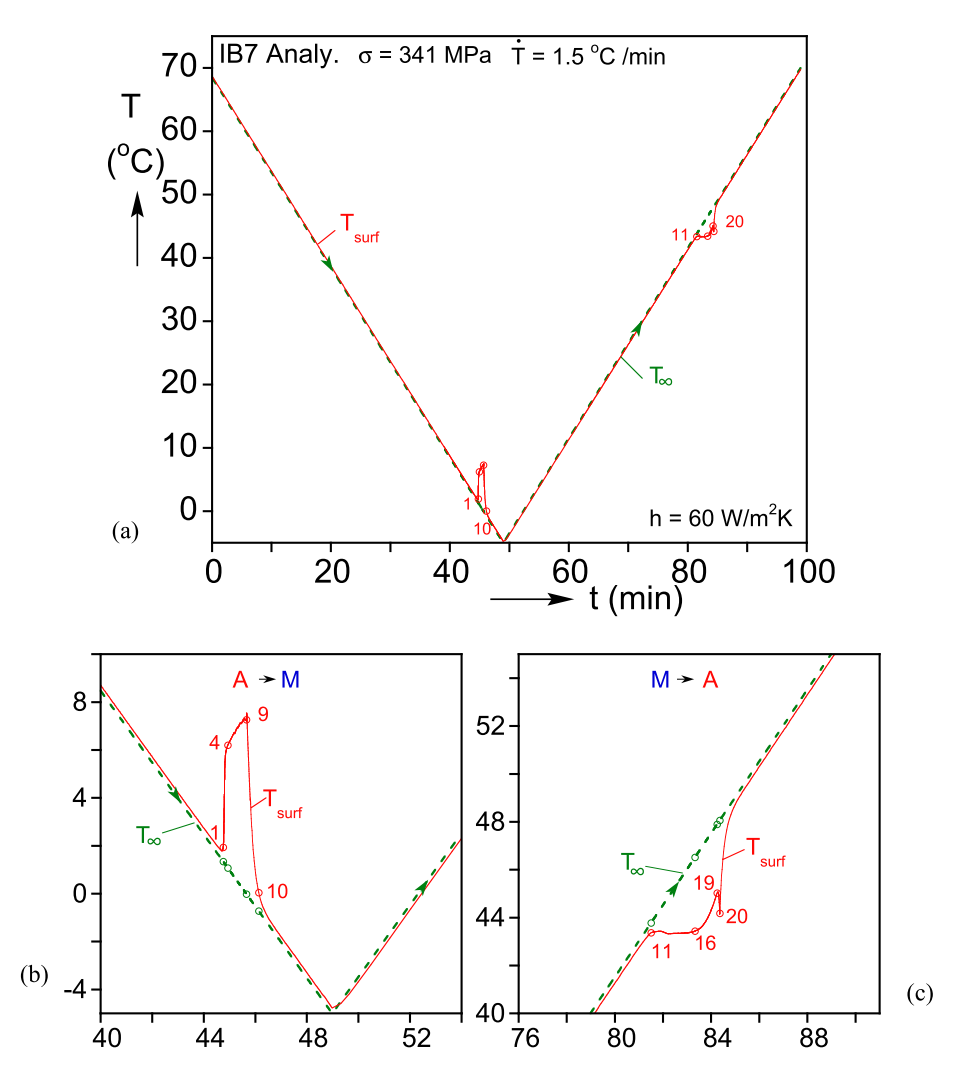


Fig. 9. Temperature-time history of the simulation of IB7. Shown are the prescribed temperature (T_{∞} , dashed line), and that calculated on the surface of the model (T_{surf} , solid line). (a) Overall histories; (b) expanded histories during the A-M transformation; (c) expanded histories during the M-A transformation.

$$\sigma_{ij\cdot j} = 0 \text{ and } C\dot{T} = kT_{,ii} - T\beta_{ij} \left(\dot{\varepsilon}_{ij} - \dot{\varepsilon}'_{ij}\right) - T\dot{S}' + 2\lambda.$$
 (13)

These are solved by the ABAQUS Standard FEA solver, employing a fully coupled backward Euler solution technique.

In the experiment, the heat exchange with the specimen is governed by the temperature-controlled airflow circulated through the small environmental chamber that surrounds it (Fig. 1). It was demonstrated that changing the velocity of the flow alters the heat transfer characteristics and speeds up or slows down the transformations. Reproducing this complex heat exchange condition by the analysis is beyond the scope of the present investigation. In the current analysis of the problem, specimen-environment heat transfer is governed strictly by the convection coefficient h in (12). In order to facilitate comparison between experimental and analytical results, h was selected so that the predicted average strain rate $(\Delta \hat{\epsilon})$ during the forward transformation matched that of Exp. IB7.

4. Simulation of 341 MPa isobaric experiments

4.1. Simulation of experiment IB7

The analysis outlined is now used to simulate the two isobaric experiments of Section 2. Starting with Exp. IB7, h is assigned the value of 60 W/m²K. The prescribed temperature history, $T_{\infty} - t$, is plotted in Fig. 9a together with the induced calculated surface temperature, $T_{surf} - t$ (T_{surf} is averaged over the outer surface of the model). T_{surf} tracks the prescribed value very well but exhibits two

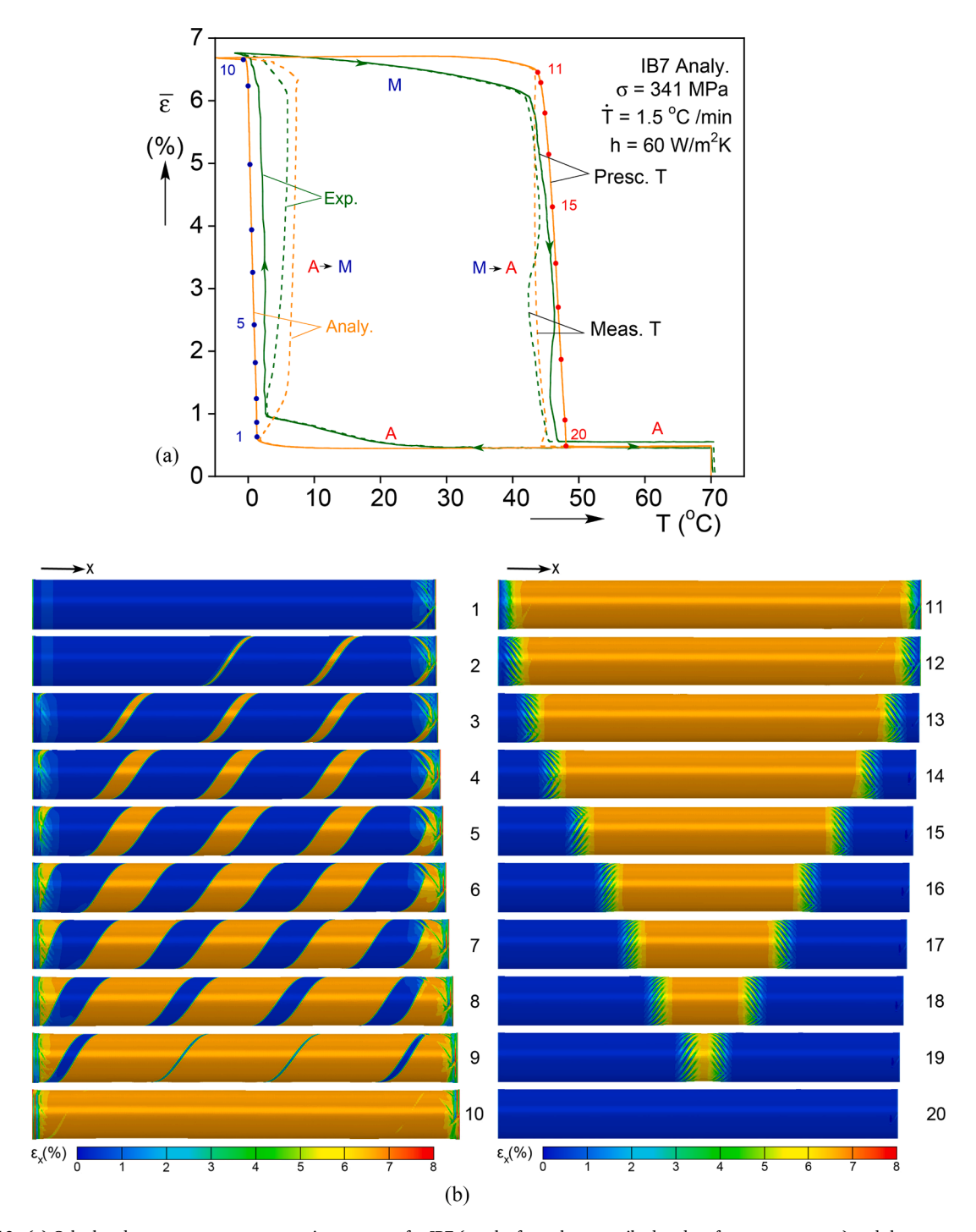


Fig. 10. (a) Calculated temperature-average strain responses for IB7 (results from the prescribed and surface temperatures) and the corresponding experimental responses. (b) Sets of calculated deformed configurations with axial strains superimposed corresponding to the A-M (left) and M-A (right) transformations.

transients during the phase transformations. Similar to the experimental results in Fig. 3, the first transient shown expanded in Fig. 9b is caused by the exothermic $A \rightarrow M$ transformation, and the second in Fig. 9c by the endothermic $M \rightarrow A$ transformation. In the analysis the inner surface of the thin-walled tube is insulated.

The two temperature records are plotted against the calculated average strain, \bar{e} , in Fig. 10a together with the corresponding experimental responses. Included are two sets of specimen deformed configurations with axial strain contours superimposed (Fig. 10b). They correspond to stations marked with solid bullets on the $T_{\infty} - \bar{e}$ response (in the analysis $\bar{e} \equiv \delta/L$). The analysis does not

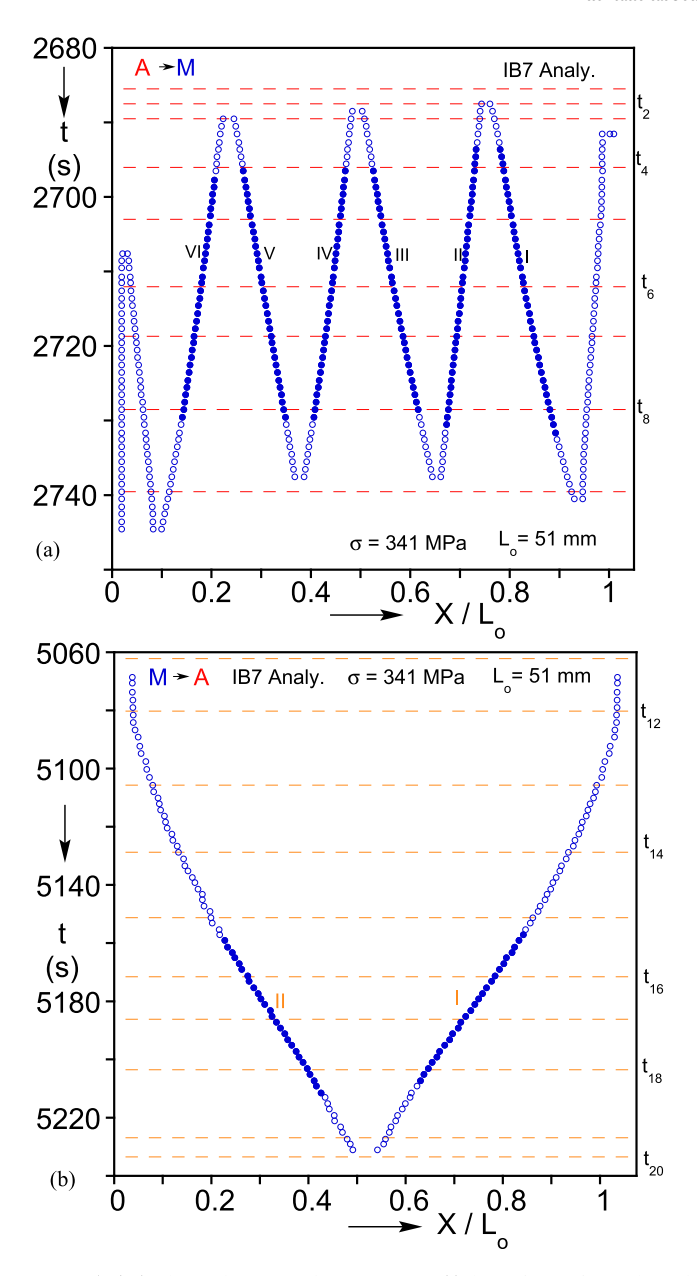


Fig. 11. Deformed configuration positions (X/L_o) of transformation fronts vs. time (t) from the analysis of IB7 for: (a) the A-M and (b) the M-A transformation.

account for the R-phase and thus during the initial decrease in temperature the predicted strain remains nearly unchanged until the onset of transformation at $T\approx 1.5~{\rm C}$ is approached. At this point the higher strain M-phase nucleates from the imperfection on the right end as a narrow band that develops into a helical band with a helix angle of about 55°. It propagates down the length of tube, simultaneously broadening (images ①-④ in Fig. 10b), mimicking the band evolution of the experiment in Fig. 4. With the onset of transformation, the measured specimen temperature follows a somewhat higher trajectory because of the released heat (corresponds to the temperature transient in Fig. 9b) and rejoins $T_{\infty} - \bar{\epsilon}$ on the completion of the transformation (station @). Interestingly, the cusp-like response observed in the experiment in Fig. 4a due to saturation of M is reproduced by the analysis.

As T_{∞} is ramped up, the strain remains nearly constant until M \rightarrow A transformation commences initially at the restrained ends. By Station m, when multi-pronged bands start to propagate from the ends toward the center of the specimen, $\bar{\epsilon}$ has been reduced to about 6.5%. As the two bands propagate toward each other the average strain is gradually reduced, and by station m the whole of the specimen is back to the A-phase and the cycle is completed. Since M \rightarrow A transformation is endothermic, in this case the surface temperature lags slightly behind the prescribed (see also the temperature transient in Fig. 9c). Video IsobTemp_StrnAna.avi provides a more detailed exposé of the evolution of transformation in the model.

Table 4 Calculated front velocities during the $A \rightarrow M$ transformation of IB7.

	μm/s					
Front No.	I	II	III	IV	V	VI
\dot{X}	149.9	-82.76	143.7	-97.84	131.1	-103.1
$rac{(\dot{X_i}-\dot{X_{i+1}})}{2}\;i=1,3,5$	116.3		120.8		117.1	
Average			1	18.1		

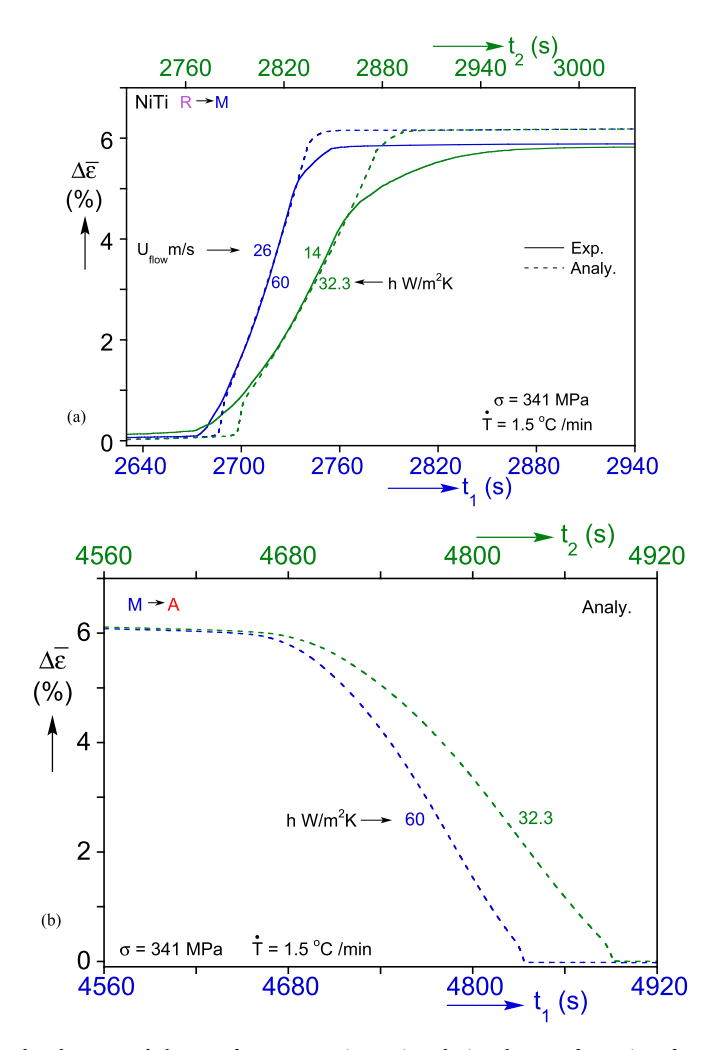


Fig. 12. Comparison of calculated and measured change of average strain vs. time during the transformations for IB7 and IB14: (a) the R-M and (b) the M-A transformation – comparison with experiments is not performed for this transformation because of differences in the localization patterns.

The axial positions of the edges of the helical band that developed during the A \rightarrow M transformation are used to generate the X-t diagram in Fig. 11a (data at 1s intervals). It exhibits a zigzag pattern very similar to that of the experiment in Fig. 5a. The velocities of the six main fronts evaluated over the intervals depicted with solid bullets are listed in Table 4. The values exhibit similar differences between forward (I, III, V) and backward (II, IV, VI) traveling fronts as in the experiment. Like in the experiment, the average velocities of the three pairs of fronts have similar values and the overall average of 118 μ m/s compares with 121 μ m/s reported in Table 2 for Exp. IB7. Overall the transformation consumed 65 s.

The X-t diagram for the two multi-pronged front propagation that developed during the $M\to A$ transformation is plotted in Fig. 11b (data at 2 s intervals). The data traces a V-shaped trajectory expected from two fronts propagating toward each other. The trajectories are somewhat curved at the early stages indicating slower propagation. They later settle into nearly steady state with velocities of about 197 μ m/s for the forward traveling front (II) and -218μ m/s for the backward propagating front (I) resulting in an average velocity of 208 μ m/s- evaluated over the intervals drawn with solid bullets. The overall time of this transformation is 175 s.

We thus once more observe that the two multi-pronged fronts propagate at much higher velocity than the rate at which the helical front broadens, but the transformations lasts significantly longer. Once more the main cause is the two-front propagation.

The calculated change in the average strain during transformation, $\Delta \bar{\epsilon}$, for the A \rightarrow M transformation is compared to the measured values in Fig. 12a. As mentioned earlier, in the analysis the value of h was chosen so that the slope of this plot matches that of the experiment, as indeed is the case in this figure. This leads to quite comparable values of front velocities. The difference in the duration of calculated and measured events – 65 s vs. 92 s – is caused by the more complex nucleation and completion of transformation in the experiment.

In the experiment the $M \to A$ transformation evolved primarily via a single propagation front. By contrast, in the analysis two multipronged propagation fronts developed. Accordingly, the front velocities are different and so are the durations of these events. Consequently, comparison of the time histories of the two $\Delta \bar{\epsilon}$ is not warranted, and Fig. 12b plots only the results of the analysis.

4.2. Simulation of experiment IB14

In this simulation h is assigned the value of 32.3 W/m²K, which corresponds to the value used in IB7 multiplied by 14/26, the ratio of the velocities of the two airflows in the experiments. Interestingly, using this ratio reproduces the slope of the $\Delta \bar{\epsilon} - t$ of IB14 (see Fig. 12a).

The results are similar to the predictions of IB7 and are only summarized here. The prescribed and calculated temperatures are plotted against the average strain in Fig. B3a together with the corresponding experimental responses. M nucleates at essentially the same temperature as in the experiment, and propagates via a helical band with a 55° helix angle (Fig. B3b). Here also, T_{surf} follows a higher temperature during the transformation than the prescribed T_{∞} . The average velocity of the edges of the band is down to 72.9 μ m/s, and consequently the transformation takes 110 s to complete, which compares with the 65s duration of the IB7 simulation.

During the heating the nucleation of M is delayed until about 43 °C compared to the 37 °C nucleation in the experiment. Similar to the analysis results of IB7, it evolves via two multi-pronged fronts that propagate from the ends toward the center. The measured temperature lags behind the prescribed value $-T_{\infty}$. The average velocity of the fronts is 157 μ m/s and the duration of this transformation is 230 s (Fig. 12b), which compares with the 175 s duration of the IB7 simulation.

Overall, the simulations demonstrate that lowering the value of the convection coefficient h, slows down the rate of transformations in a manner similar to reducing the airflow velocity in the experiments.

5. Summary and concluding remarks

The paper introduced a custom, small-scale testing facility for thermomechanical experiments on SMA materials and simple structures that undergo phase transformation under accurately controlled thermal and mechanical loadings at different rates. The facility was subsequently used to thermally cycle NiTi tubes under constant stress of 341 MPa, monitoring the temperature and full field deformation. The experiment starts at 70 °C with the material in the A-phase. The temperature is lowered at the rate of 1.5 °C/min inducing transformation at 25 °C to the R-phase and at 3 °C to the M-phase. The deformation associated with the A \rightarrow R transformation of about 0.5% is homogeneous. However, the nearly 6% change in strain associated with the R \rightarrow M transformation localizes into a narrow helical band that first propagates along the length and then broadens. This transformation takes 92 s and the speed at which the helical band broadens follows the relationship $\dot{X} = \dot{\delta}/n\Delta\varepsilon^t$. Upon the completion of this transformation, the temperature is increased at the same rate. The specimen deforms uniformly until at 43 °C it starts transforming back to A. The associated reduction in strain localizes into a single multipronged front that propagates at a much higher speed. The transformation takes 209 s, the deformation is fully recovered, and the $T-\bar{\varepsilon}$ hysteresis closes. The following additional observations can be made from the experiments.

- The small size of the chamber, the precise feedback control of the temperature and load, and the full-field monitoring of the deformation of the specimen enable a sharper determination of the transformation temperatures, a more complete understanding of the associated banded localizations, the speeds of their evolution, and their relationship to the problem parameters.
- Although helical bands propagate at much slower speeds than single multi-pronged fronts, they transform the specimen in a shorter time because of the multiplicative effect of the broadening of the helical band.
- A significant finding is that heat transfer is governed by the airflow through the environmental chamber. By changing the airflow
 velocity it was demonstrated that the propagation of transformation fronts slows down or accelerates so as to match the rate at
 which heat is removed/added by the slower/faster airflow.
- Under the well-controlled conditions of the experiment, temperature changes induced by the latent heats are minimized keeping
 the specimen temperature close to the prescribed path.
- The complex thermomechanical interactions reported place a high bar on any analysis and associated constitutive model; thus the
 experiment provides a demanding platform for evaluating their performance.

The recent extension of the phenomenological constitutive model developed by our group for the thermomechanical demands of the present problem (A&L2022a) is implemented as a material subroutine (UMAT) and used in a FE analysis to simulate the experiments. Novel features of the constitutive model include: the reversible $A \rightleftharpoons M$ transformation is modeled through a single surface in the s-T space that obeys kinematic hardening; the transformation strain and entropy are the internal variables whose evolution is

governed by an associative flow rule; and the inhomogeneous deformation exhibited in tension is modeled as softening. The model is calibrated to measured isothermal tensile responses in the temperature regime of interest with softening introduced over the upper and lower stress plateaus. Additional parameters were provided by the thermoelastic properties of the material. The latent heat was evaluated from the transformation stress-temperature relationship by employing the Clausius-Clapeyron equation.

An important aspect of the current analysis is that heat exchange between the model tube and the "environment" is limited to convection. As a result, the speed of propagation of transformation fronts is proportional to $h(T-T_{\infty})/q_l$ (h is the convection coefficient and q_l the latent heat of transformation). Thus, the convection coefficient h was selected so that the calculated rate of average transformation strain in the analysis matches that of the $R \rightarrow M$ transformation of Exp. IB7.

The model tube is discretized with a mesh fine enough to reproduce the finer features of the anticipated localization patterns. It is taken through the same cool/heat history as that of Exp. IB7. The temperature-strain response is accurately reproduced by the analysis with the two transformations initiating at essentially the same temperatures as in the experiment. The $A\rightarrow M$ transformation is in the form of a helical band of about 6.5% strain that nucleates from a local thickness depression on the moving end of the model (the R-phase is not included in the constitutive model). The helical band propagates and broadens at about the same average speed as in the experiment. Whereas in the experiment the $M\rightarrow A$ transformation was primarily through a single multipronged front, in the analysis two multipronged fronts developed that propagated from the two ends to the center of the model. We attribute this difference primarily to differences in boundary conditions and geometric and other imperfections not included in the analysis. Although the speed of the two fronts is higher than the average helical band broadening speed, the overall time of this transformation is longer. Additional observations follow.

- The rather complex thermomechanical interactions resulting from the $A \rightleftharpoons M$ transformations that take place in these isobaric experiments provided insights that guided the implementation of the constitutive model in the FE analysis, and enabled the successful reproduction of the main features of the problem.
- At the same time, since in the analysis heat exchange between the model tube and the "environment" is strictly by convection, the
 convection coefficient had to be chosen by matching the rate of average transformation rate in this analysis to that of the experiment. In such experiments the heat exchange is much more complex requiring a more elaborate heat transfer modeling.
- The initiation of transformation and the resultant deformation patterns are influenced by the boundary conditions of the structure
 and by small imperfections in the specimen and setup. In the analysis these were addressed by radially constraining the two ends of
 the model, and by the small thickness depression introduced at the moving end.
- The analysis reproduced the slower flow experiment (IB14) quite successfully by reducing the value of the convection coefficient by the same ratio as that of the two flow speeds of the experiment.
- Overall, reproduction of the complex behavior observed in these experiments required that all aspects of the analysis: the calibration of the constitutive model, its discretization and numerical implementation into a UMAT, and the FE analysis of the structure had to be executed to near perfection. The generally good reproduction of all aspects of experiments demonstrates the fidelity of the constitutive and structural models, and points to required improvements. At the same time, this novel contribution to the field informs other analysts on what is required for modeling complex thermomechanical interactions of SMAs.

Declaration of Competing Interest

None.

Data availability

Data will be made available on request.

Acknowledgments

The authors acknowledge with thanks the financial support received for this work from the National Science Foundation under grant no. CMMI-1762389. The literature on thermomechanics of shape memory alloys is vast, so mainly articles that influenced our work are cited.

Supplementary materials

Supplementary material associated with this article can be found, in the online version, at doi:10.1016/j.ijplas.2023.103567.

Appendix A. Motion of coexisting phase boundaries

Following Abeyaratne and Knowles (2006), consider a bar of length L, fixed at x=0 and stretched by a displacement δ at x=L. It develops a stress, σ , at which two phases coexist, with strains ε_L and ε_H . Two fronts separate the two phases, as shown in the inset in Fig. A1, located at s_1 and s_2 propagating in opposite directions. In terms of the deformed coordinates

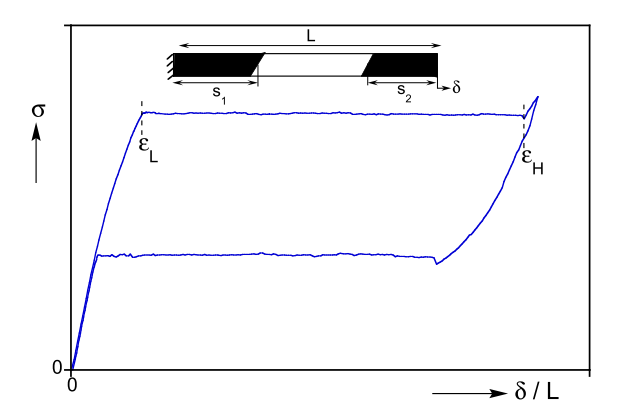


Fig. A1. Kinematics of coexisting transformation fronts.

$$X_1 = s_1 + u(s_1) = s_1(1 + \varepsilon_H),$$
 (A.1a)

and

$$X_2 = (L - s_2) + u(L - s_2) = (L - s_2) + u(s_1) + (L - s_1 - s_2)\varepsilon_L.$$
(A.1b)

The velocity of the fronts is then

$$\dot{X}_1 = \dot{s}_1(1 + \varepsilon_H),\tag{A.2a}$$

$$\dot{X}_2 = -\dot{s}_2(1 + \varepsilon_L) + \dot{s}_1(\varepsilon_H - \varepsilon_L),\tag{A.2b}$$

and

$$\dot{X}_1 - \dot{X}_2 = (\dot{s}_1 + \dot{s}_2)(1 + \varepsilon_L).$$
 (A.3)

The end displacement

$$u(L) = \delta = (s_1 + s_2)\varepsilon_H + (L - s_1 - s_2)\varepsilon_L, \tag{A.4}$$

and the velocity

$$\dot{u}(L) = \dot{\delta} = (\dot{s}_1 + \dot{s}_2)(\varepsilon_H - \varepsilon_L). \tag{A.5}$$

If $\dot{s}_1 = \dot{s}_2$ then $\dot{s} = \frac{\dot{\delta}}{2\Delta \varepsilon^i}$ (i.e., Eq. (1) Shaw and Kyriakides, 1997)

In terms of deformed coordinate velocities

$$\dot{\delta} = (\dot{X}_1 - \dot{X}_2) \left(\frac{\varepsilon_H - \varepsilon_L}{1 + \varepsilon_L} \right). \tag{A.6}$$

Appendix B. Experimental and Simulation Results for IB14

Fig. B1a plots the prescribed and measured temperature-average strain $(T - \bar{\epsilon})$ responses for IB14. Fig. B1b shows two sets of specimen deformed configurations corresponding to the two phase transformations with axial strain contours superimposed. Fig. B2 plots the prescribed and measured temperature histories for the IB14 experiment.

Figure B3a plots the calculated $T - \bar{\epsilon}$ responses and the corresponding experimental ones; Fig. B3b presents the corresponding specimen deformed configurations during the two phase transformations.

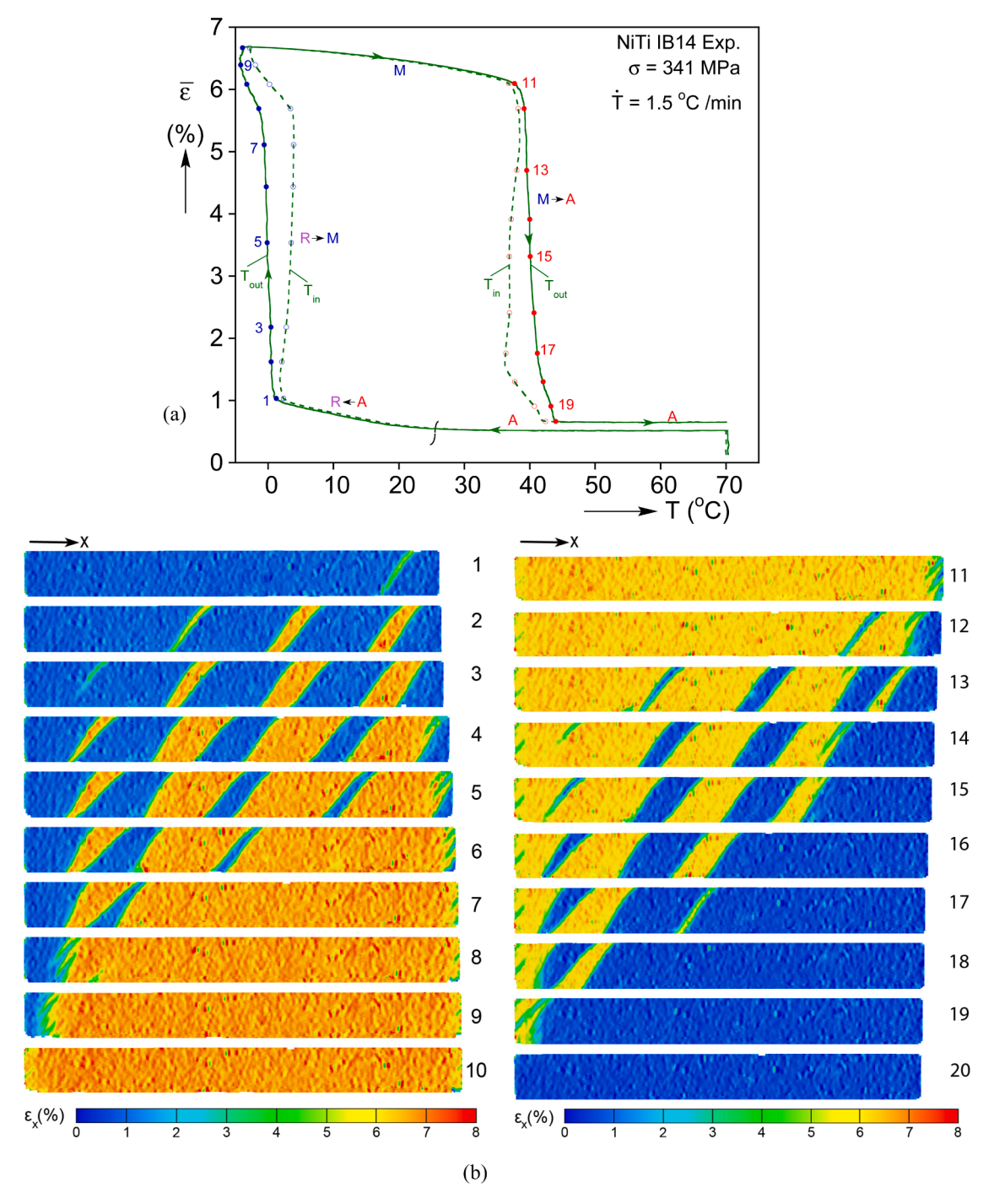


Fig. B1. (a) Temperature-average strain responses recorded in Exp. IB14 (temperatures from the outer and inner thermocouples). (b) Sets of specimen deformed configurations with axial strains superimposed corresponding to the R-M (left) and M-A (right) transformations.

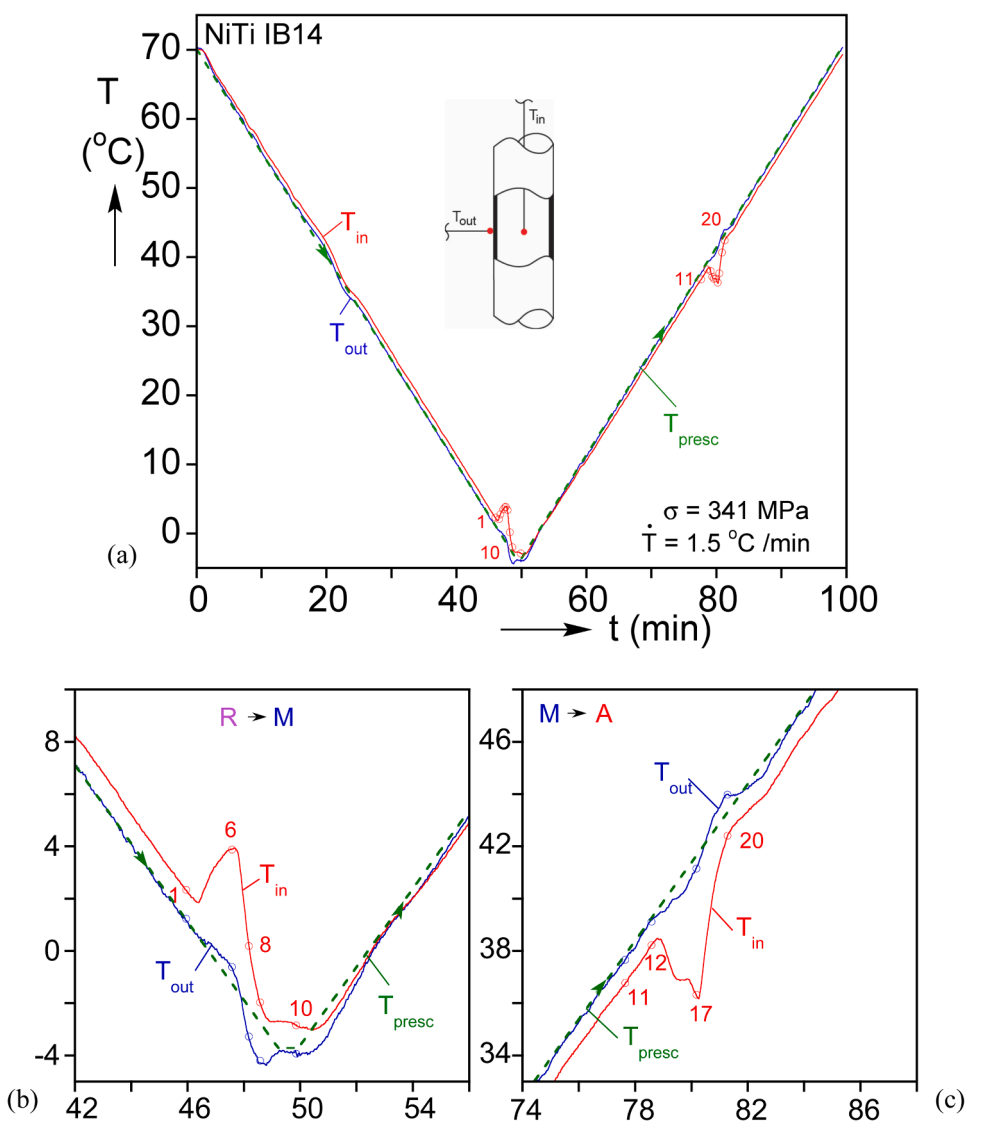


Fig. B2. Temperature-time history of Exp. IB14. Shown are the prescribed temperature (dashed line), and those recorded by the outer and inner thermocouple (solid lines). (a) Overall histories; (b) expanded histories during the R-M transformation; (c) expanded histories during the M-A transformation.

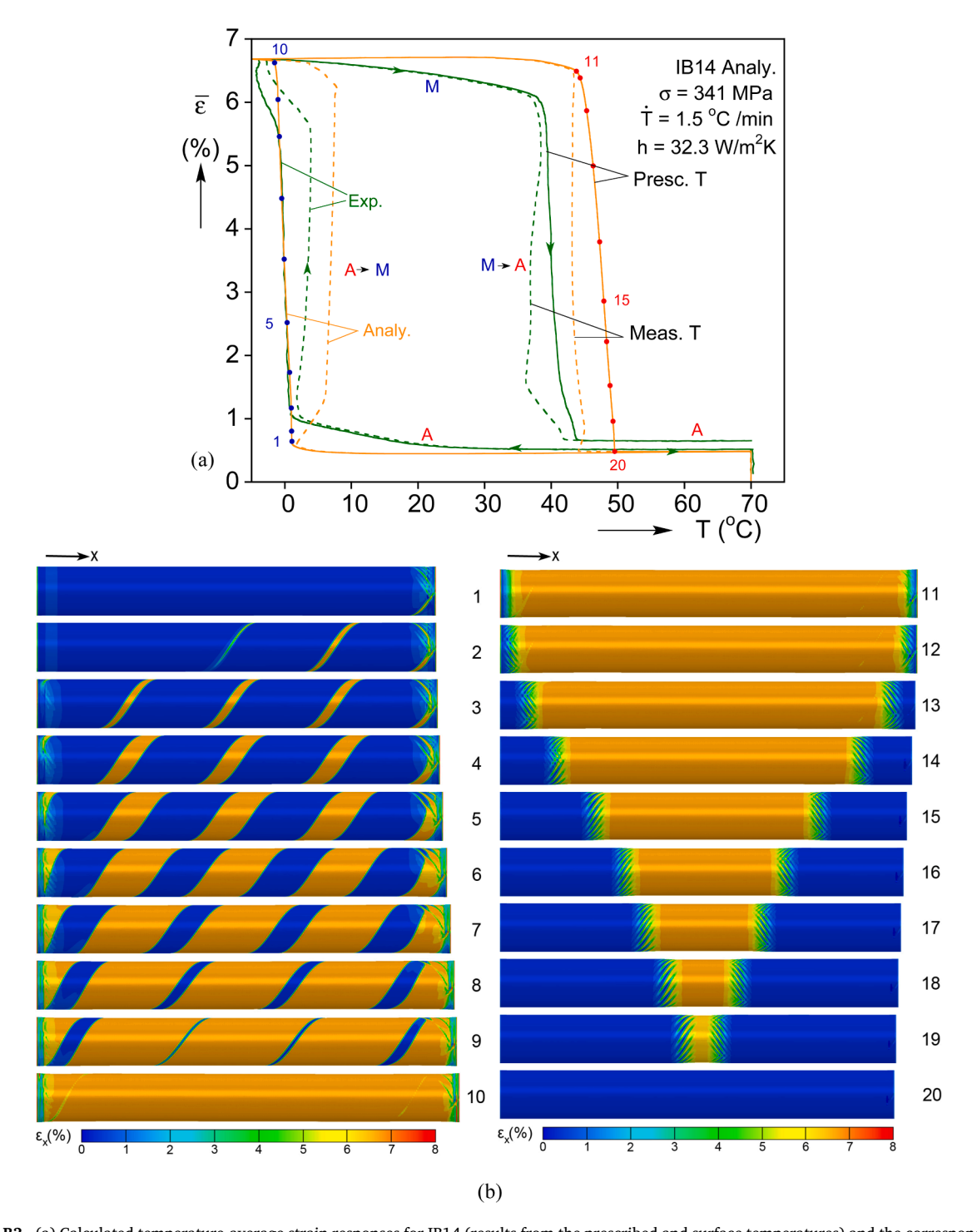


Fig. B3. (a) Calculated temperature-average strain responses for IB14 (results from the prescribed and surface temperatures) and the corresponding experimental responses. (b) Sets of calculated deformed configurations with axial strains superimposed corresponding to the A-M (left) and M-A (right) transformations.

Appendix C. Model calibration

The transformation potential adopted is

$$\Psi^{I} = \frac{H(\overline{\varepsilon}^{I}/\varepsilon_{o})^{2}}{2\left(1 - \frac{\overline{\varepsilon}^{I}}{\varepsilon_{o}} - \frac{\overline{S}^{I}}{S_{o}}\right)^{n}} + \frac{H_{1}}{\left(1 - \frac{S^{I}}{S_{o}}\right)^{u}\left(\frac{S^{I}}{S_{o}}\right)^{v}} + \theta^{*}S^{I} + \frac{H_{2}}{2}\left[\left(1 - \frac{S^{I}}{S_{o}}\right)^{2} + \left(\frac{S^{I}}{S_{o}}\right)^{2}\right]. \tag{C.1}$$

The present application of the constitutive model outlined in Section 3.1 is limited to the pseudoelastic behavior of NiTi in tension. Furthermore, the calibration of the constitutive model is based on two isothermal uniaxial tension experiments corresponding to the extreme temperatures of the 341 MPa isobaric experiment presented in Section 2.1 plotted in Fig. C1 (i.e., 40 °C and 3 °C). The results are used to construct the linear transformation stress-temperature plots in Fig. C2.

- ε_0 is assigned the value of the extent of the transformation plateau as shown in Fig. C1.
- The denominator of the first term of the transformation potential Ψ^t is constructed so as to ensure that ε^t and S^t evolve in an analogous manner see Fig. C3). The exponent, n, controls the stiffness of this asymptote (Section 4.2, A&L2022a).
- The $A \to M$ and $M \to A \sigma^t \theta$ lines are extrapolated down to $\sigma = 0$ and the distance between the intercepts is $2\theta_0$. The parameter θ^* is the average temperature of the two intercepts with $\sigma = 0$ (Fig. C2).

The Clausius-Clapeyron equation for reversible phase transformations is

$$\frac{d\sigma}{d\theta}\Big|_{\epsilon} = -\frac{\ell^{\epsilon}}{\theta \Delta \varepsilon^{i}},\tag{C.2}$$

where ℓ^t is the latent heat of transformation, and Δe^t is the transformation strain (e.g., Otsuka and Shimizu, 1986; Ahadi and Sun, 2013; Pataky et al., 2015; Duerig et al., 2017; Grassi et al., 2020). For the present isothermal transformations the apparent transformation heat, r, includes the latent heat as well as the heat dissipation due to the hysteresis traced, i.e.,

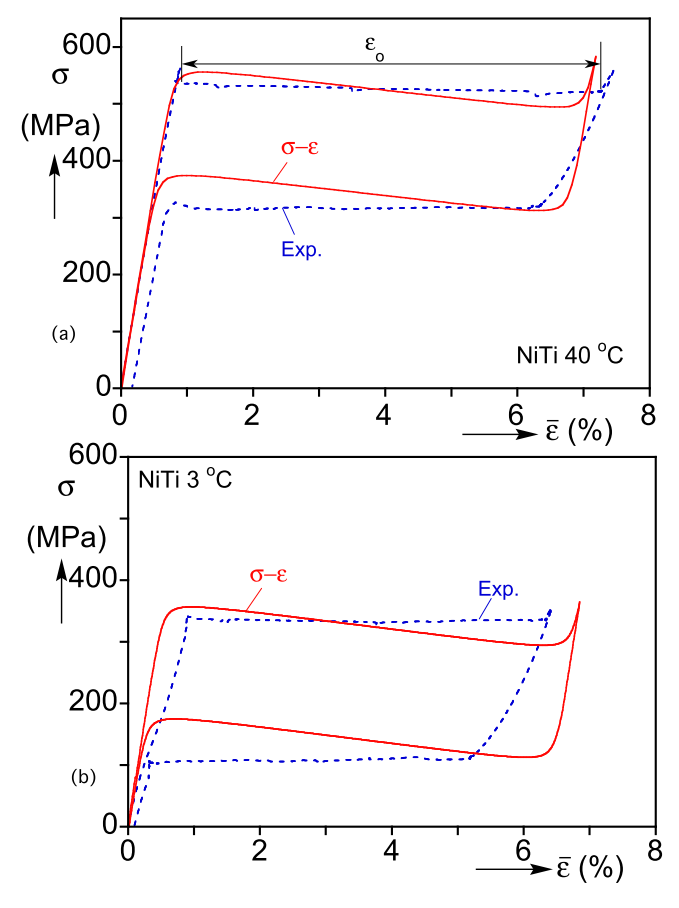


Fig. C1. Measured and fitted isothermal stress-strain responses: (a) at 40 $^{\circ}$ C and (b) at 3 $^{\circ}$ C.

$$r_{A \to M} = \int_{A}^{M} (\theta \dot{S}' - 2\lambda) d\tau = -\theta S_o - 2\Delta \lambda, \tag{C.3a}$$

and

$$r_{M\to A} = \int_{M}^{A} (\theta \dot{S}^{t} - 2\lambda) d\tau = \theta S_{o} - 2\Delta \lambda. \tag{C.3b}$$

Here $2\Delta\lambda$ is the hysteretic contribution to the heat – included in typical DSC measurements. In the present calibration this term is small compared to the first term and will be neglected. The calibration slopes of the transformations then become

$$\frac{d\sigma}{d\theta}\Big|_{tA\to M} \approx \frac{S_o}{\varepsilon_o} \approx \left. \frac{d\sigma}{d\theta} \right|_{tM\to A},$$
(C.4)

which allows estimation of S_0 (see Fig. C2).

- The thermoelastic properties of A and M are assumed to be the same and take the values in Table C1 (elastic modulus, E, Poisson's ratio, ν , coefficient of thermal expansion, α , specific heat, C/ρ , mass density, ρ , thermal conductivity, k). The R-phase is not included in the model.
- The pseudoelastic behavior of NiTi is modeled by softening slopes over the extents of the transformations (assumed to be the same for loading and unloading e.g., Shaw and Kyriakides, 1998; Kyriakides and Miller, 2000; Hallai and Kyriakides, 2013; Jiang et al., 2016b, 2017a). The softening slopes and their transitions are represented as follows:
- The hardening/softening slope is governed primarily by H_2 .
- The quadratic terms in the square bracket ensure that the Maxwell stress is at the level of the measured propagation stress independently of *H*₂.
- The shapes of the transitions to softening and saturation are governed by the saturation exponents $\{u, v\}$ in the second term (typically take the same value in order to preserve the level of the Maxwell stress).

The values of these parameters are determined for best fit of the pseudoelastic stress-average strain response at 40 °C shown in Fig. C1a. The parameters chosen are listed in Table C2 and the resultant stress-strain response is included in Fig. C1a.

Figure C1b compares the model response to the experimental one at 3 °C. The constitutive model does not account for the R-phase and this is responsible for the difference in the initial rising part of the response from the measured one. Furthermore, the strain extent of the predicted transformation is longer than the measured value.

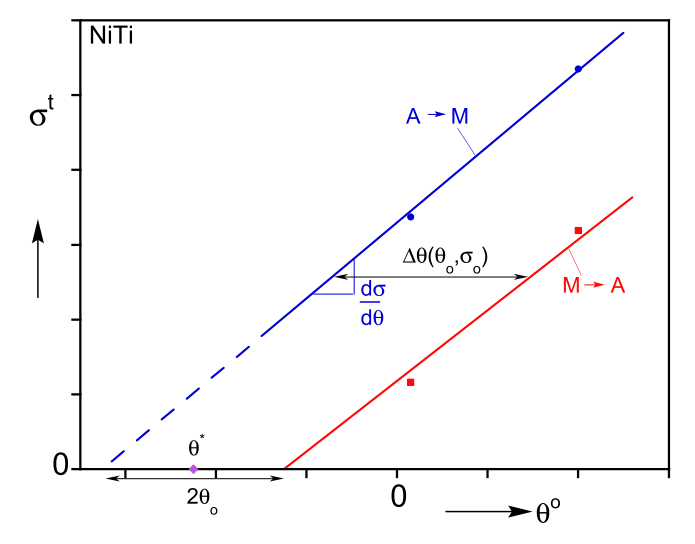


Fig. C2. Linear transformation stress-temperature fits based on the isothermal experiments in C1, extrapolated to zero stress; marked are several parameters of the constitutive model.

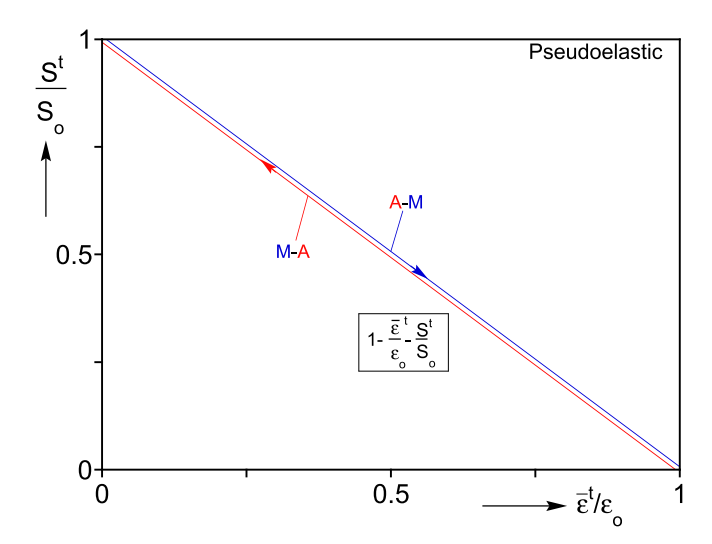


Fig. C3. Asymptotic relationships between the transformation entropy and transformation strain.

Table C1Thermoelastic properties of NiTi used in the analysis.

Phase	E GPa	ν	$\frac{\alpha}{K}$ – 1	C/ρ J/kgK	$ ho m kg/m^3$	k W/mK
A/M	73	0.425	10^{-5}	320	6450	18

Table C2Model calibration variables.

σ_o MPa	θ _o K	ε _ο %	S _o MPa/K	θ* K	u,v	n	H MPa	H ₁ MPa	H ₂ MPa
80	8	6.17	0.332	233.5	0.01	0.1	0.38	2.8	-3

References

Abeyaratne, R., Knowles, J.K., 2006. Evolution of Phase Transformations: A continuum Theory. Cambridge University Press, New York, NY. https://doi.org/10.1017/CBO9780511547133.

Ahadi, A., Sun, Q., 2013. Stress hysteresis and temperature dependence of phase transition stress in nanostructured NiTi—Effects of grain size. Appl. Phys. Lett. 103, 021902 https://doi.org/10.1063/1.4812643.

Alsawalhi, M.Y., Landis, C.M., 2022a. A new phenomenological constitutive model for shape memory alloys. Int. J. Solids Struct. 257, 111264 https://doi.org/10.1016/j.ijsolstr.2021.111264.

Alsawalhi, M.Y., Landis, C.M., 2022b. On the fracture toughness of shape memory alloys. Int. J Fract 236, 201–218. https://doi.org/10.1007/s10704-022-00648-w. Alsawalhi, M.Y., 2022. Phenomenological Constitutive Modeling and Numerical Analysis of Fracture Toughness for Shape Memory Alloys. PhD Dissertation, Engineering Mechanics, Univ., Texas at Austin https://doi.org/10.26153/tsw/42995.

Arghavani, J., Auricchio, F., Naghdabadi, R., Reali, A., Sohrabpour, S., 2010. A 3-D phenomenological constitutive model for shape memory alloys under multiaxial loadings. Int'l J. Plast. 26, 976–991. https://doi.org/10.1016/j.ijplas.2009.12.003.

ASTM E3097-17, 2018. Standard methods for mechanical uniaxial constant force thermal cycling of shape memory alloy. In: https://www.astm.org/e3097-17.html. Baxevanis, T., Parrinello, A.F., Lagoudas, D.C., 2016. On the driving force for crack growth during thermal actuation of shape memory alloys. J. Mech. and Phys. Solids 89, 255–271. https://doi.org/10.1016/j.jmps.2015.12.011.

Bechle, N.J., Kyriakides, S., 2014. Localization in NiTi tubes under bending. Int. J. Solids Struct. 51, 967–980. https://doi.org/10.1016/j.ijsolstr.2013.11.023. Bechle, N.J., Kyriakides, S., 2016a. Evolution of localization in pseudoelastic NiTi tubes under biaxial stress states. Int. J. Plasticity 82, 1–31. https://doi.org/10.1016/j.ijplas.2016.01.017.

Bechle, N.J., Kyriakides, S., 2016b. Evolution of phase transformation fronts and associated thermal effects in a NiTi tube under a biaxial stress state. Extreme Mech. Lett. 8, 55–63. https://doi.org/10.1016/j.eml.2016.02.018.

Boyd, J.G., Lagoudas, D.C., 1996. A thermodynamic constitutive model for the shape memory alloy materials. Part I. the monolithic shape memory alloy. Int. J. Plasticity 12, 805–842. https://doi.org/10.1016/S0749-6419(96)00030-7.

Daly, S., Ravichandran, G., Bhattacharya, K., 2007. Stress-induced martensitic phase transformation in thin sheets of Nitinol. Acta Mat. 55, 3593–3600. https://doi.org/10.1016/j.actamat.2007.02.011.

Duerig, T.W., Bhattacharya, K., 2015. The influence of the R-phase on the superelastic behavior on NiTi. Shap. Mem. Superela. 1, 153–161. https://doi.org/10.1007/s40830-015-0013-4.

Duerig, T.W., Pelton, A.R., Bhattacharya, K., 2017. The measurement and interpretation of transformation temperatures in Nitinol. Shap. Mem. Superela. 3, 485–498. https://doi.org/10.1007/s40830-017-0133-0.

Favier, D., Louche, H., Schlosser, P., Orgéas, L., Vacher, P., Debove, L., 2007. Homogeneous and heterogeneous deformation mechanisms in an austenitic polycrystalline Ti–50.8 at % Ni thin tube under tension. Investigation via temperature and strain fields measurements. Acta Mat 55, 5310–5322. https://doi.org/10.1016/j.actamat.2007.05.027.

Frost, M., Benešová, B., Seiner, H., Kružík, M., Šittner, P., Sedlák, P., 2021. Thermomechanical model for NiTi-based shape memory alloys covering macroscopic localization of martensitic transformation. Int. J. Solids Struct. 221, 117–129. https://doi.org/10.1016/j.ijsolstr.2020.08.012.

- Gibbs, J.W., 1878. On the equilibrium of heterogeneous substances. Am. J. Sci. s3-16, 441-458. https://doi.org/10.2475/ajs.s3-16.96.441.
- Grassi, E.N.D., Chagnon, G., de Oliveira, H.M.R., Favier, D., 2020. Anisotropy and Clausius-Clapeyron relation for forward and reverse stress-induced martensitic transformations in polycrystalline NiTi thin walled tubes. Mech. Mater. 146, 103392 https://doi.org/10.1016/j.mechmat.2020.103392.
- Hallai, J.F., Kyriakides, S., 2011. On the effect of Lüders bands on the bending of steel tubes: part II analysis. Int. J. Solids Struct. 48, 3285–3294. https://doi.org/10.1016/j.jisolstr.2011.07.012.
- Hallai, J.F., Kyriakides, S., 2013. Underlying material response for Lüders-like instabilities. Int. J. Plasticity 47, 1–12. https://doi.org/10.1016/j.ijplas.2012.12.002. Hill, R., 1952. On discontinuous plastic states, with special reference to localized necking in thin sheets. J. Mech. Phys. Solids 1, 19–30. https://doi.org/10.1016/
- Iadicola, M.A., Shaw, J.A., 2002. An experimental setup for measuring unstable thermo-mechanical behavior of shape memory alloy wire. J. Intel. Mat. Syst. Struct. 13, 157–166. https://doi.org/10.1177/104538902761402558.
- Iadicola, M.A., Shaw, J.A., 2004. Rate and thermal sensitivities of unstable transformation behavior in a shape memory alloy. Int. J. Plast 20, 577–605. https://doi.org/10.1016/S0749-6419(03)00040-8.
- Jacobus, K., Sehitoglu, H., Balzer, M., 1996. Effect of stress state on the stress-induced martensitic transformation of polycrystalline Ni-Ti Alloy. Metal. Mater. Trans. A 27, 3066–3073. https://doi.org/10.1007/BF02663855.
- Jiang, D., Bechle, N.J., Landis, C.M., Kyriakides, S., 2016a. Buckling and recovery of NiTi tubes under axial compression. Int. J. Solids Struct. 80, 52–63. https://doi.org/10.1016/j.ijsolstr.2015.10.022.
- Jiang, D., Landis, C.M., Kyriakides, S., 2016b. Effects of tension/compression asymmetry on the buckling and recovery of NiTi tubes under axial compression. Int. J. Solids Struct. 100–101 41–53. https://doi.org/10.1016/j.ijsolstr.2016.07.003.
- Jiang, D., Landis, C.M., 2016. A constitutive model for isothermal pseudoelasticity coupled with plasticity. Shape Mem. Superelast. 2, 360–370. https://doi.org/10.1007/s40830-016-0078-8.
- Jiang, D., Kyriakides, S., Landis, C.M., 2017a. Propagation of phase transformation fronts in pseudoelastic NiTi tubes under uniaxial tension. Extreme Mech. Lett. 15, 113–121. https://doi.org/10.1016/j.eml.2017.06.006.
- Jiang, D., Kyriakides, S., Bechle, N.J., Landis, C.M., 2017b. Bending of pseudoelastic NiTi tubes. Int. J. Solids Struct. 124, 192–214. https://doi.org/10.1016/j. ijsolstr.2017.06.032.
- Kazinakis, K., Kyriakides, S., Jiang, D., Bechle, N.J., Landis, C.M., 2021. Buckling and collapse of pseudoelastic NiTi tubes under bending. Int. J. Solids Struct. 221, 2–17. https://doi.org/10.1016/j.ijsolstr.2019.12.017.
- Kazinakis, K., Kyriakides, S., Landis, C.M., 2022. Simulation of the response and evolution of localization in pseudoelastic NiTi tubes under biaxial stress states. Int'l J. Plast. 151, 103179 https://doi.org/10.1016/j.ijplas.2021.103179.
- Kyriakides, S., Miller, J.E., 2000. On the propagation of Lüders bands in steel strips. ASME J. Appl. Mech. 67, 645–654. https://doi.org/10.1115/1.1328348.
- Lagoudas, D.C., 2008. Shape Memory Alloys: Modeling and Engineering Applications. Springer, New York, NY. https://doi.org/10.1007/978-0-387-47685-8. Lagoudas, D., Hartl, D., Chemisky, Y., Machadov, L., Popov, P., 2012. Constitutive model for the numerical analysis of phase transformation in polycrystalline shape memory alloys. Int. J. Plast. 32–33. 155–183. https://doi.org/10.1016/j.jiplas.2011.10.009.
- Levitas, V.I., Ozsoy, I.B., 2009a. Micromechanical modeling of stress-induced phase transformations. Part 1. Thermodynamics and kinetics of coupled interface propagation and reorientation. Int. J. Plast. 25, 239–280. https://doi.org/10.1016/j.ijplas.2008.02.004.
- Levitas, V.I., Ozsoy, I.B., 2009b. Micromechanical modeling of stress-induced phase transformations. Part 2. Computational algorithms and examples. Int. J. Plast. 25, 546–583. https://doi.org/10.1016/j.ijplas.2008.02.005.
- Lexcellent, C., Boubakar, M.L., Bouvet, C., Calloch, S., 2006. About modelling the shape memory alloy behaviour based on the phase transformation surface identification under proportional loading and anisothermal conditions. Int. J. Solids Struct. 43, 613–626. https://doi.org/10.1016/j.ijsolstr.2005.07.004.
- Li, M., Chen, M., Sun, Q., 2021. Nonlocal modeling and analysis of spatiotemporal patterns in non-isothermal phase transformation in NiTi strips. Int. J. Solids Struct. 221, 103–116. https://doi.org/10.1016/j.ijsolstr.2020.05.013.
- Li, Z.Q., Sun, Q.P., 2002. The initiation and growth of macroscopic martensite band in nano-grained NiTi microtube under tension. Int. J. Plasticity 18, 1481–1498. https://doi.org/10.1016/S0749-6419(02)00026-8.
- Mao, S., Luo, J., Zhang, Z., Wu, M., Liu, Y., Han, X., 2010. EBSD studies of the stress-induced B2-B19' martensitic transformation in NiTi tubes under uniaxial tension and compression. Acta Mater. 58, 3357–3366. https://doi.org/10.1016/j.actamat.2010.02.009.
- Orgéas, L., Favier, D., 1998. Stress-induced martensitic transformation of a NiTi alloy in isothermal shear, tension and compression. Acta Mater. 46, 5579–5591. https://doi.org/10.1016/S1359-6454(98)00167-0.
- Otsuka, K., Shimizu, K., 1986. Pseudoelasticity and shape memory effects in alloys. Int. Met. Rev. 31, 93–114. https://doi.org/10.1179/imtr.1986.31.1.93. Otsuka, K., Wayman, C.M., 1999. Shape Memory Materials. Cambridge University Press, Cambridge, UK. https://www.cambridge.org/us/academic/subjects/engineering/materials-science/shape-memory-materials?format=PB&isbn=9780521663847.
- Pataky, G.J., Ertekin, E., Sehitoglu, H., 2015. Elastocaloric cooling potential of NiTi, Ni2FeGa, and CoNiAl. Acta Mater. 96, 420–427. https://doi.org/10.1016/j.actamat.2015.06.011.
- Reedlunn, B., Churchill, C.B., Nelson, E.E., Shaw, J.A., Daly, S.H., 2014. Tension, compression, and bending of superelastic shape memory tubes. J. Mech. Phys. Solids 63, 506–537. https://doi.org/10.1016/j.jmps.2012.12.012.
- Reedlunn, B., LePage, W.S., Daly, S.H., Shaw, J.A., 2020. Axial-torsion behavior of superelastic tubes: part I, proportional isothermal experiments. Int. J. Solids Struct. 199, 1–35. https://doi.org/10.1016/j.ijsolstr.2020.03.018.
- Rezaee-Hajidehi, M., Tůma, K., Stupkiewicz, S., 2020. Gradient-enhanced thermomechanical 3D model for simulation of transformation patterns in pseudoelastic shape memory alloys. Int. J. Plast. 128, 102589 https://doi.org/10.1016/j.ijplas.2019.08.014.
- Sedlak, P., Frost, M., Benešova, B., Ben Zineb, T., Šittner, P., 2012. Thermomechanical model for NiTi-based shape memory alloys including R-phase and material anisotropy under multi-axial loadings. Int. J. Plast. 39, 132–151. https://doi.org/10.1016/j.iiplas.2012.06.008.
- Shaw, J.A., Kyriakides, S., 1995. Thermomechanical aspects of NiTi. J. Mech. Phys. Solids 43, 1243-1281. https://doi.org/10.1016/0022-5096(95)00024-D.
- Shaw, J.A., Kyriakides, S., 1997. On the nucleation and propagation of phase transformation fronts in a NiTi alloy. Acta Mater. 45, 683–700. https://doi.org/10.1016/S1359-6454(96)00189-9.
- Shaw, J.A., Kyriakides, S., 1998. Initiation and propagation of localized deformation in elasto-plastic strips under uniaxial tension. Int. J. Plast. 13, 837–871. https://doi.org/10.1016/S0749-6419(97)00062-4.
- Sun, Q.P., Li, Z.Q., 2002. Phase transformation in superelastic NiTi polycrystalline micro-tubes under tension and torsion—from localization to homogeneous deformation. Int. J. Solids Struct. 39, 3797–3809. https://doi.org/10.1016/S0020-7683(02)00182-8.
- Valanis, K.C., 1970. On the thermodynamic foundation of classical plasticity. Acta Mech. 9, 278-291. https://doi.org/10.1007/BF01179826.